

# The presence of transparent exopolymer particles rather than ballast determines sinking of small particles during late summer in the Northeast Pacific Ocean

Elisa Romanelli<sup>1</sup>, Julia Sweet<sup>1</sup>, Sarah Lou Carolin Giering<sup>1</sup>, David Siegel<sup>1</sup>, and Uta Passow<sup>1</sup>

<sup>1</sup>Affiliation not available

May 25, 2023

Elisa Romanelli <sup>1</sup>, Julia Sweet <sup>2,3</sup>, Sarah Lou Carolin Giering <sup>4</sup>, David A. Siegel<sup>1</sup>, Uta Passow <sup>2,5</sup>

<sup>1</sup> Earth Research Institute, University of California, Santa Barbara, CA, United States

*elisa.romanelli@lifesci.ucsb.edu*, *david.siegel@ucsb.edu*

<sup>2</sup> Marine Science Institute, University of California, Santa Barbara, CA, United States

<sup>3</sup> University of Louisiana at Lafayette, LA, United States

*julia.sweet1@louisiana.edu*

<sup>4</sup> National Oceanography Centre, Southampton, United Kingdom

*s.giering@noc.ac.uk*

<sup>5</sup> Memorial University, St John's, Canada

*uta.passow@mun.ca*

## Corresponding author

Elisa Romanelli

Interdepartmental Graduate Program in Marine Science

University of California

Santa Barbara, CA

*elisa.romanelli@lifesci.ucsb.edu*

## Abstract

Gravitational sinking of particles is a key pathway for the transport of particulate organic carbon (POC) to the deep ocean. Particle size and composition influence particle sinking velocity and thus play a critical role in controlling particle flux. Canonically, sinking particles that reach the mesopelagic are expected to be either large, or ballasted by minerals. However, the presence of transparent exopolymer particles (TEP), which are positively buoyant, may also influence particle sinking velocity. We investigated the relationship between particle composition and sinking velocity during the EXPORTS campaign (Export Processes in the Ocean from RemoTe Sensing) in the Northeast Pacific Ocean using Marine Snow Catchers. Suspended and sinking

particles were sized using the FlowCam and their biogeochemical composition was assessed by measuring the concentration of particulate organic carbon (POC) and nitrogen, particulate inorganic carbon, biogenic and lithogenic silica and TEP. Sinking fluxes were also calculated. Overall, suspended and sinking particles were small ( $< 51 \mu\text{m}$ , diameter) in this late summer, oligotrophic system. Contrary to expectation, the ratio of ballast minerals to POC was higher for suspended particles than sinking particles. Further, suspended particles showed TEP-to-POC ratios three times higher than sinking particles. This suggests that TEP content dictated the sinking behavior of the two particle fractions. Fluxes of POC averaged to  $4.3 \pm 2.5 \text{ mmol C m}^{-2}\text{d}^{-1}$  at 50 m and decreased to  $3.1 \pm 1.1 \text{ mmol C m}^{-2} \text{ d}^{-1}$  at 300–500 m. These flux estimates were slightly higher than fluxes measured during EXPORTS with drifting sediment traps and Thorium-234. A comparison between these approaches illustrates that small sinking particles were an important component of the POC flux in the mesopelagic of this late summer oligotrophic system.

## 1. Introduction

The biological carbon pump (BCP) comprises the processes that mediate the transfer of organic carbon from the euphotic zone, where it is produced, to the deep ocean (Volk and Hoffert, 1985). Without the BCP the concentrations of atmospheric  $\text{CO}_2$  would be  $\sim 200$  ppm higher than present (Parekh et al., 2006). The efficiency of the BCP depends primarily on the gravitational settling of particles, physical advection and mixing of particles, and the active vertical transport of particles due to migrating zooplankton and fish (Boyd et al., 2019). These processes shape the flux of carbon and other elements through the mesopelagic and abyssopelagic zones, where carbon can be locked away from the atmosphere, impacting atmospheric  $\text{CO}_2$  concentrations over climatologically relevant timescales (Kwon et al., 2009; DeVries et al., 2012). Accurately predicting the response of the ocean carbon storage to already underway and future climate changes requires a mechanistic knowledge of the processes making up the BCP (e.g., Siegel et al., 2023).

The largest component of the BCP is settling particles (Boyd et al., 2019; Nowicki et al., 2022). Particles in the open ocean are mainly produced in the surface ocean and consist of living and dead phytoplankton cells, detritus, carcasses, fecal material, and minerals. Their size range spans between less than a micrometer (typical threshold defined as  $0.7 \mu\text{m}$  in diameter) to many millimeters, with those with a diameter of  $> 0.5$  mm being referred to as “marine snow” (Alldredge and Silver, 1988). The fate and distribution of particles are influenced by the transformation processes that change a particle’s size, composition and, consequently, sinking velocity. Particles can aggregate, disaggregate, solubilize or be remineralized back to inorganic forms via mechanical forcing, bacterioplankton activity, and interaction with zooplankton (Stemmann et al., 2004; Burd et al., 2010; Giering et al., 2014; Collins et al., 2015). When particles aggregate or are repackaged into fecal matter, they have the potential to sink rapidly ( $\sim 50$  to  $[?] 2,000 \text{ m d}^{-1}$ ) and hence more easily escape consumption, fragmentation, and dissolution at shallow depths; thus, bringing organic matter to the deep ocean more efficiently than smaller particles (Alldredge and Silver, 1988; Ebersbach and Trull, 2008).

Particle sinking velocities are typically thought to be largely determined by size. Stokes’ Law, which quantifies the sinking velocity of spherical solid particles under laminar flow conditions, assumes that particle sinking velocity increases as the product of the spherical particle’s diameter squared and the excess density with respect to seawater. The implication for sinking particles in the ocean is that large particles should sink fast and are hence effective vectors for carbon transport to depth, whereas small particles sink slow and are remineralized within the upper mesopelagic, contributing little to BCP-mediated ocean carbon storage (Kriest, 2002; Marsay et al., 2015; Cavan et al., 2017). Nevertheless, the presence of small particles ( $0.2\text{--}20 \mu\text{m}$ ) has been observed at great depths ( $> 1000$  m) (e.g., Dall’Olmo and Mork, 2014; Briggs et al., 2020). Furthermore, recent studies have shown that the downward flux of particulate organic carbon (POC) via small particles ( $< 100 \mu\text{m}$ ) can be significant in specific ecosystems and seasons, at times constituting the bulk of the total POC flux through the mesopelagic (e.g., Durkin et al., 2015; Giering et al., 2016; Bisson et al., 2020; Dever et al., 2021).

The presence of ballast minerals (biogenic silica from diatoms, particulate inorganic carbon from coccol-

ithophores and foraminifera, and lithogenic material from aeolian and riverine inputs) is also thought to increase particle sinking velocity by increasing particle excess density in respect to seawater (Armstrong et al., 2002; Passow and De La Rocha, 2006; Laurenceau-Cornec et al., 2019; Iversen and Lampitt, 2020; Iversen, 2023). However, cause and effect in the relationship between organic matter and minerals are not clear, and sinking aggregates originating from biological activity in the mixed layer could scavenge and subsequently transport small, suspended mineral particles to depth (Passow, 2004).

The presence of transparent exopolymer particles (TEP; Alldredge et al., 1993) also has the potential to influence the sinking of particles. TEP are largely composed of polysaccharides released by phytoplankton and bacteria as extracellular surface-active exopolymers (Passow, 2002), especially under nutrient-limited conditions (Obernosterer and Herndl, 1995). TEP may act as biological glue and thus enhance particle coagulation rate by increasing particle "stickiness" (Passow et al., 1994; Jackson, 1995). However, by being positively buoyant, TEP may also reduce aggregates' sinking velocities especially when aggregates are characterized by high TEP-to-solid particles ratio (Engel and Schartau, 1999; Azetsu-Scott and Passow, 2004). Although TEP has the potential to play an important role in controlling the downward transport of particles, we lack a robust mechanistic understanding of this process (e.g., Mari et al., 2017; Nagata et al., 2021).

Our hypothesis is that TEP play a critical role in determining the sinking velocity of particles, potentially outcompeting the role of ballast minerals. We assess how particle size and composition regulates the partitioning between sinking and suspended particles within the upper mesopelagic in an iron-limited region of the Northeast Pacific Ocean. Particles were collected during the EXPORTS (Export Processes in the Ocean from RemoTe Sensing) field campaign using Marine Snow Catchers (MSC). Finally, we discuss the possible mechanisms driving the formation of small sinking particles in the mesopelagic and highlight the importance of studying small particle characteristics and particle patchiness to enhance our understanding of the functioning of the biological carbon pump.

## 2. Materials and Methods

### 2.1 Ocean Station Papa

This study is part of the first EXPORTS field campaign, which took place in late summer 2018 (August 14 to September 9) at Ocean Station Papa ('Station P'). Station P is a time-series site located in the Northeast Pacific Ocean (nominally 50°N 145°W) that has been regularly monitored since 1949 (e.g., Tabata 1965). It is a high-nutrient and low-chlorophyll system with a 'muted' spring bloom owing to persistently low concentrations of iron (Martin and Fitzwater, 1988; Boyd et al., 1996). During our study, Station P was characterized by a shallow mixed layer (average:  $29 \pm 4$  m), and strong vertical and weak horizontal gradients in hydrographic properties (Siegel et al., 2021). Mixed layer macronutrient concentrations were elevated and chlorophylla concentrations were low with a mean of  $0.21 \mu\text{g L}^{-1}$ , which was less than typical August values (2000–2017) for Station P (Siegel et al., 2021). This condition resulted in an isolume depths of the 1% photosynthetically available radiation (PAR) between 70 to 90 m (mean:  $78 \pm 6$  m) (Siegel et al., 2021), which was slightly deeper than climatological conditions (Siegel et al., 2021). The site was characterized by a highly recycled food web in the mixed layer (Meyer et al., 2020; McNair et al., 2023), with low POC fluxes (Buesseler et al., 2020; Estapa et al., 2021), which were in line with previous observations performed at Station P (Charette et al., 1999; Wong et al., 2002; Kawakami et al., 2010; Timothy et al., 2013; Mackinson et al., 2015). An in-depth discussion of how POC fluxes measured during EXPORTS compare to previous POC flux measurements is provided in Buesseler et al., (2020).

The observations presented here were conducted from the R/V *Roger Revelle*, which sampled ecological and biogeochemical properties following an instrumented Lagrangian Float drugged at  $\sim 100$  m depth. A detailed operational description of the EXPORTS North Pacific field campaign can be found in Siegel et al., (2021).

## 2.2 Sample collection with the Marine Snow Catchers

Profiles of suspended and sinking particles were collected using three Marine Snow Catchers (MSC; Lampitt et al., 1993, OSIL, UK). The MSC is a large volume (volume:  $V_{\text{MSC}} = 89.8$  L, height:  $h_{\text{MSC}} = 1.5$  m) water sampler with a removable base section ( $\sim 8$  L) that enables the partitioning of particles according to a predefined settling time (Riley et al., 2012; Giering et al., 2016). The MSCs were deployed at two to three depths ranging between 20 and 500 m at 13 stations (**Table S1**). Deployment depths were chosen to include (1) just below the mixed layer depth (20–65 m), (2) at  $\sim 100$  m (Lagrangian float depth), and (3) between 100–500 m. Depths were adjusted to match where particle maxima were detected immediately before the MSC deployments, either via chlorophyll fluorescence profile, or particle counts from the Underwater Vision Profiler-5 (Picheral et al., 2010, Hydroptic, FR). MSC casts were conducted in the afternoons on days 1, 3, and 6 of each of the three 8-day sampling epochs, with additional two-depths casts on days 5 of epochs 2 and 3 (**Table S1**).

A full description of the MSC and its sampling methodology has been published by Riley et al. (2012) and Giering et al. (2016). We modified the protocol slightly as follows: During deployment, the terminal apertures of the top and base sections of the MSC were kept open and were closed at the target depth through a wire-guided messenger trigger mechanism. A tray (height:  $h_{\text{tray}} = 4.4$  cm, area:  $A_{\text{tray}} = 0.028$  m<sup>2</sup>, approximate volume:  $\sim 1$  L) was placed at the bottom of the MSC base section prior to each deployment. Immediately following deployment and retrieval, the MSC was secured in an upright position, the initial bulk population of particles was sampled from the MSC’s central tap (time zero,  $T_0$ ), and particles were allowed to settle for 2 hours. We operationally defined three particle fractions, *top* ( $t$ ), *base* ( $b$ ) and *tray* ( $tr$ ) according to their sampling location within the MSC after the 2-hour settling period. The *top* fraction was collected from the central tap in the top section of the MSC and represents the suspended particle pool, i.e., particles that did not sink during the 2 hours settling period. Subsequently, the water contained in the upper part of the MSC was gently drained, and the upper part of the MSC removed. The water in the base section overlying the tray was siphoned off, constituting the *base* fraction (volume:  $V_{\text{base}}$ ; 4.5–5.5 L). Water in the tray was considered as the *tray* fraction (volume:  $V_{\text{tray}}$  0.33–0.98 L). The *base* and *tray* sampled volumes varied across deployments depending on sampling efficiency (i.e., how much volume was lost during sampling). In the laboratory, the tray was visually investigated for the presence of marine-snow-sized particles. In two instances (settling time experiments, see section 2.6) the *tray* and *base* fraction were combined before sampling (referred to as *bottom* fraction).

All three fractions (*top*, *base*, *tray*) were subsampled for various parameters (**Table S1**). Subsamples for particulate organic carbon and nitrogen (POC and PON) analysis and for counts and identification (particle imaging via the FlowCam) were collected at all stations, except on August 17 when no samples were fixed. Subsamples for the analysis of total particulate carbon (TC), from which we obtained particulate inorganic carbon estimates (PIC) by difference ( $\text{PIC} = \text{TC} - \text{POC}$ ), biogenic and lithogenic silica (bSi and lSi, respectively) were taken on days 3 and 5 of each epoch. Subsamples for the determination of TEP were collected on days 1 and 5 of each epoch, and the abiotic aggregation potential was determined on seawater collected on day 1 of each epoch.

## 2.3 Particle imaging and sizing with the FlowCam

Particle size distribution of suspended and sinking particles was assessed using particle imaging. Subsamples (50 mL) were fixed with 37% formalin (hexamethylenetetramine buffered) to a final concentration of 1–2% and stored in dark at 4°C until analysis. Subsamples were analyzed using a FlowCam 8000 Series (Sieracki et al., 1998, Yokogawa Fluid Imaging Technologies, US) in auto-image mode (particles imaged at a pre-defined flow rate) (**Table S2**). To assess relevant particle sizes, we first analyzed subsamples using a x40 objective combined to a 300x1500- $\mu\text{m}$  flow cell and then a x200 objective with a 50x300- $\mu\text{m}$  flow cell. Note that 13 out of 30 suspended particle samples were not analyzed with the x40 objective due to time constraints. The minimum sizes reliably resolved by the objectives were 30  $\mu\text{m}$  and 3  $\mu\text{m}$ , respectively. The maximum size was dictated by the flow cell size and was 300  $\mu\text{m}$  for the x40 objective and 50  $\mu\text{m}$  for the x200 objective. *Base*

and *tray* fractions were pre-filtered using a 44- $\mu\text{m}$  mesh filter to avoid clogging the 50x300- $\mu\text{m}$  flow cell when using the x200 objective.

Based on the size of the particles and the FlowCam resolution, we chose to restrict our analysis to particles with an Equivalent Spherical Diameter (ESD) between 4 and 128  $\mu\text{m}$ . We calculated the minimum number of particles required to estimate a robust particle size spectrum using the empirical relationship given by Blanco et al. (1994) and assuming that a size bin is well represented if there are at least 10 particles in it (Álvarez et al., 2011). Thus, we imaged around 1,300 particles (i.e., minimum desired count and lowest number of counted particles) to cover a size range of 4 to < 32  $\mu\text{m}$  at x200 and a size range of [?] 32 to 128  $\mu\text{m}$  at x40.

Imaged particles were sized using FlowCam’s VisualSpreadsheet© software version 4.15.1. and grouped in the five size bins based on their ESD. The complete method settings and example images are presented in **Table S2**. Particle concentrations of *top*, *base* and *tray* were calculated by dividing the counted number of particles in each size bin by the sample volume imaged. Suspended and sinking particle abundances were calculated as explained in section 2.7. Particle size distributions (PSDs) were estimated as differential number size distributions  $N(D)$  (# particle  $\text{mL}^{-1}\mu\text{m}^{-1}$ ) for *top* and *tray* fractions. The slope of the PSDs was calculated as the slope of a one-degree polynomial fit to the  $\log_{10}$ -transformed PSD and  $\log_{10}$ -transformed arithmetic mean of each size bin ( $\mu\text{m}$ ) over the entire measured size range (polyfit function, Matlab R2021b).

## 2.4 Biogeochemical analyses

Typically, 1 L of the  $T_0$ , *top* and *base* fractions and  $\sim 0.1$  L of the *tray* fraction were filtered each for analysis of POC and PON, TC, bSi and lSi, and TEP. For the occasions when we carried out the settling time methodological test, between 0.5–1.5 L of the *top* and *bottom* subsamples were filtered instead.

Concentrations of POC and PON were determined by filtering subsamples onto two replicate pre-combusted (450 °C, 30 minutes) GF/F filters (25 mm, Whatmann, UK). The filters were dried at 60°C and stored at room temperature until analysis. Filters were analyzed using a CEC 440HA elemental analyzer (Control Equipment, US) after treatment with 10% HCl. Replicates were averaged (see average of the relative standard deviations of the filter replicates in **Table S3**). Detection limit of POC and PON ranged between 0.8–16  $\mu\text{g}$  and 0.2–3.9  $\mu\text{g}$ , respectively. All POC values were above the detection limit of the instrument. However, for PON, 24 of 237 values were below detection, seven of which were negative and therefore substituted with zero ( $\mu\text{g L}^{-1}$ ). Values were corrected to account for non-target carbon on the filter using the average POC and PON mass (12.6  $\mu\text{g}$  for POC; 2.1  $\mu\text{g}$  for PON) of 28 blanks obtained using a multiple volume (0.5, 1 and  $\sim 2$ L) regression approach (Moran et al., 1999) of water collected with Niskin Bottles from the CTD-rosette system within the mixed layer (campaign-wide correction). A detailed explanation of the blank correction method and a reconciliation of all the POC and PON measurements obtained using different methodologies during the EXPORTS field campaign is presented by Graff et al., (*in review*).

Total particulate carbon (TC) was measured following procedures similar to POC but without prior acidification. Only one filter per fraction was generated due to volume constraints. No measured values fell below the instrument detection limit (1.2 to 4.5  $\mu\text{g}$ ). Particulate inorganic carbon (PIC) was calculated by subtracting the uncorrected POC from TC.

Biogenic and lithogenic silica concentrations were determined by filtering samples onto 0.6- $\mu\text{m}$  pore size polycarbonate membrane filters (47 mm diameter, Isopore, Millipore), which were dried at 60°C and stored at room temperature until analysis. Filters were digested in Teflon tubes by adding 4 mL of 0.2 N (normal) NaOH (95°C, 40 minutes) and cooled immediately afterwards. The resulting solutions were neutralized by adding 1 mL of 1 M (molar) HCl and centrifuged (10 minutes, 2500 rpms) to separate lSi from bSi. 4 mL of the solution was diluted with 6 mL of Milli-Q water and assessed via the molybdosilicic acid spectrophotographic method to measure bSi (Strickland and Parsons, 1968). The remaining 1 mL of solution, which was left at the bottom of the Teflon tube together with the filter, was rinsed using Milli-Q water, left to dry, and cooled. To extract lSi, 0.25 mL of 2.5 M (molar) hydrofluoric acid were added. After 48 hours 9.75 mL

1 M (molar) saturated boric acid solution were added, and filters were centrifuged. 8 mL of the resulting solution was added to 2 mL 1 M (molar) saturated boric acid solution and assessed spectrophotometrically as aforementioned.

Concentrations of TEP were determined colorimetrically on triplicate samples. Subsamples were filtered onto 0.4- $\mu\text{m}$  pore size polycarbonate filters (25 mm, Whatmann, UK), stained with Alcian blue, and stored frozen until analysis. Filter blanks, prepared by staining and rinsing wet filters, were processed like the samples. Stained filters were soaked for at least 2 hours in 80% sulfuric acid (Fisher Scientific; 95% w/w), and the absorption at 787 nm was measured spectrophotometrically (Thermo Scientific GENESYS 10S UV- VIS; Passow and Alldredge, 1995). The stained filters were compared to a standard curve developed using Gum Xanthan (Sigma-Aldrich) and hence TEP determinations were expressed as standardized Gum Xanthan equivalents (GXeq) (Bittar et al., 2018). TEP determinations were considered above detection, if the absorbance value of a sample at 787 nm was at least twice the absorbance value of the blank at 787 nm (Passow and Alldredge, 1995). A total of 28 of 112 TEP determinations measured from the MSC were below this detection limit. TEP associated with sinking particles between 300 and 500 m was always at or below detection limit. In addition to the MSC samples, we also determined water column TEP concentration on water collected using Niskin bottles fitted to a CTD rosette (depth range: 5–500 m;  $n = 153$ ). A total of 22 of 153 TEP measured on the water column sampled with the Niskin bottles were at or below the detection limit. We did not remove TEP values at or below the limit of detection but consider these observations an upper bound estimate of the real in situ concentrations. We expressed TEP in carbon units (TEP-C) using a conversion factor of 0.75  $\mu\text{g C } \mu\text{g L}^{-1} / \text{GXeq L}^{-1}$  (Engel and Passow, 2001).

Several values of the biogeochemical measurements were considerably higher than the average concentrations at their collection depth. This occurred for  $\sim 5\%$  of the total number of observations and these samples are referred to here as *outliers*. Outliers were defined as observations that were at least twice the average concentration for that depth layer. We refer to background concentrations when these outliers were removed to assess the baseline biogeochemical composition of suspended and sinking particles. The nature of the outliers and the implication of their presence is discussed in section 4.5 below.

## 2.5 Abiotic aggregation potential experiments

The potential for the abiotic formation of aggregates was evaluated using rolling tanks experiments. Four experiments were conducted using MSC  $T_o$  (August 25 at 95 m), *top* (August 25 at 95 m) or *base* (August 17 at 55 m and August 19 at 55 and 95 m) sample fractions. Each experiment was conducted for 36 hours in 1.1-L rolling tanks at near *in situ* temperature (13°C or 4°C) in the dark. Aggregate formation was monitored by visually checking every 6 hours for the appearance of marine snow-sized particles (ESD > 0.5 mm).

## 2.6 Settling time experiments for MSC

Methodological experiments to determine the effect of settling time on particle fractions partitioning were conducted twice (on August 20 and September 03, **Table S1**) from MSC deployments at 60 and 80 m depth, respectively. Each time, all three MSCs were deployed at the same depth, but settling times after retrieval varied: particles were allowed to settle for 1, 2 and 4 hours after recovery of the MSCs. Subsamples of *top* and *bottom* fractions were analyzed for POC and PON, bSi and TEP.

## 2.7 Calculations of particle concentrations and fluxes

Following Riley et al. (2012) and Giering et al. (2016), concentrations of suspended ( $c_{\text{NS}}$ ), slow-sinking ( $c_{\text{SS}}$ ) and fast-sinking ( $c_{\text{FS}}$ ) particles were calculated as follows:

$$c_{\text{NS}} = \textit{top} \text{ concentration } (2)$$

$$c_{\text{SS}} = (\textit{base} - \textit{top} \text{ concentrations}) \times V_{\textit{base}} / V_{\text{MSC}} (3)$$

$$c_{FS} = (\text{tray} - \text{base concentrations}) \times V_{\text{tray}} / (A_{\text{tray}} \times h_{\text{MSC}}) \quad (4)$$

Occasionally, after applying the corrections we obtained negative values i.e., the *top* concentration exceeded the *base* concentration, or the *base* concentration exceeded the *tray* concentration. We assigned a zero concentration to the specific observations. The negative values could reflect a lack of sinking particles, the presence of ascending particles and/or actively moving zooplankton. In the analyses that follow, little differences were found between slow- and fast-sinking particle concentrations (see section 3.2). Hence, these two sinking particle fractions are combined. In four deployments, TEP and TC were measured only in the *top* and *tray* fractions. In these cases, sinking TEP and TC concentrations were estimated following equation (4) but subtracting the *top* fraction from the *tray* fraction.

The standard particle sinking velocity for the MSC is assumed to be  $18 \text{ m d}^{-1}$  as determined geometrically by dividing the sinking distance (height of the MSC;  $h_{\text{MSC}} = V_{\text{MSC}} / A_{\text{MSC}} = 1.5 \text{ m}$ ) by the settling time ( $t = 2 \text{ hours}$ ). We assumed that the  $18 \text{ m d}^{-1}$  sinking velocity estimate for sinking particles represents a lower bound estimate because the sinking particles could have reached the bottom of the MSC much sooner (Giering et al., 2016).

## 2.8 Statistical analyses

The relative uncertainties in the calculated concentrations and fluxes were determined by using a Monte Carlo error propagation with mean values obtained by averaging the replicate filters and the precision estimated by calculating the average of the relative standard deviations of the filter replicates (**Table S3**). A 1% uncertainty was assumed for the measured values ( $V_{\text{MSC}}$ ,  $A_{\text{tray}}$ ,  $h_{\text{MSC}}$ ,  $V_{\text{base}}$ ,  $V_{\text{tray}}$ ,  $h_{\text{MSC}}$  and sinking time). Final estimates of the averages and standard deviations of particle concentrations and fluxes were then calculated from the simulation results. Simple linear regression was used to test (Student’s t-test, 95% confidence) for statistically significant temporal and depth trends displayed by the biogeochemical content of suspended, sinking particles and their partitioning to total. The linear analyses were performed using the function `fitlm` in Matlab (R2021b). The same approach was performed to test for significant temporal trends displayed by the biogeochemical content of suspended and sinking particles during the settling tests. Paired t-test was used to test for differences among particle fractions. The data presented in this study, and all the data generated during the first EXPORTS field campaign can be found at NASA SeaBASS data repository (<https://seabass.gsfc.nasa.gov/cruise/EXPORTSNP>).

## 3. Results

### 3.1 Marine snow and abiotic aggregation potential

No visible sinking marine snow particles (diameter  $> 0.5 \text{ mm}$ ) were found in the tray from any of the MSCs deployments. This observation suggests that the concentration of sinking marine-snow-sized particles was less than 0.02 per L. This finding is consistent with particle size distribution data from the UVP (pers. comm. Andrew McDonnell, 2021). Furthermore, during the four aggregation potential experiments, no visible marine snow-sized aggregates formed in the rolling tanks regardless of depth (55 and 95 m) and sample fraction (*top* or *base*).

### 3.2 Particle concentrations and size

Most of the imaged particles (were smaller than  $16 \mu\text{m}$  in diameter (ESD), whether suspended or sinking (**Figure 1**). Furthermore, particle concentrations measured in the tray were equal or lower than the ones measured in the base for 20 out of 30 MSC deployments. These observations suggest that the concentration differences between *base* and *tray* particle fractions were too small to be detected with this method. We hence summed the concentrations of slow- and fast-sinking particles into a single sinking particle fraction. This

decision is additionally supported by the lack of marine snow, which would have contributed appreciably to the fast-sinking particle fraction.

Our results, based on the analysis of particles with diameters (ESD) between 4 and 128  $\mu\text{m}$ , suggest that > 70% of suspended and sinking particles had a diameter of 4–8  $\mu\text{m}$ , and that particles larger than 32  $\mu\text{m}$  were at the detection limit of our method (i.e., too rare to be quantified). The partitioning of particles across the size bins was consistent among particle fractions (paired t-test,  $p = 0.33$ – $0.63$ ,  $n = 17$ ), indicating that suspended and sinking particles were similarly sized (**Figure 1** and **Table S4**).

Additionally, we calculated the particle size distribution (PSD, 4–128  $\mu\text{m}$ ) of suspended particles and of sinking (*‘tray’*) particles (uncorrected fraction) to assess differences in slopes among fractions with depth. Overall, throughout the entire water column, PSD slopes of suspended particles were similar ( $-3.3 \pm 0.3$ ) to those of sinking particles ( $-3.5 \pm 0.2$ ; **Figure S1**). Yet below 100 m, PSDs of sinking particles were significantly steeper than those of suspended particles (paired t-test,  $p = 0.03$ ,  $n = 5$ ; **Figure S1**). Furthermore, the slope of suspended PSD became significantly shallower with depth between 20 and 500 m ( $R^2 = 0.3$ ,  $p < 0.02$ ,  $n = 17$ ), while the slopes of sinking PSDs remained constant ( $R^2 = 0$ ;  $p = 0.79$ ,  $n = 17$ ; **Figure S1**).

It is important to note that the determination of particle size using this approach is associated with uncertainties due to samples handling. We cannot exclude the possibility that fragile and larger aggregates (ESD < 0.5 mm) may have broken up due to physical disturbance developed during the sampling and partitioning of the three particle fractions and during injection of samples in the FlowCam flowcell used in combination with the x40 objective (minimum size of 300  $\mu\text{m}$ ). Therefore, the size characterization performed with the FlowCam must be taken with caution. Lastly, particle type and shape could not be reliably resolved with the FlowCam due to the small size of the particles.

### 3.3 Biogeochemical partitioning by particle sinking fraction

The background suspended POC concentrations decreased significantly with depth in the euphotic zone between 20 and 65 m ( $R^2 = 0.43$ ,  $p = 0.03$ ,  $n = 11$ ) and in the upper mesopelagic between 95 and 500 m ( $R^2 = 0.59$ ,  $p = 0.001$ ,  $n = 14$ ) (**Figure 2A**), whereas background sinking POC concentrations did not significantly attenuate with depth ( $R^2 = 0$ ,  $p = 0.61$ ,  $n = 24$ ). The relative contribution of background suspended POC to total background POC decreased significantly in the upper mesopelagic ( $R^2 = 0.70$ ,  $p < 0.001$ ,  $n = 13$ ), resulting in a concomitant increase in the contribution of the background sinking POC ( $R^2 = 0.70$ ,  $p < 0.001$ ,  $n = 13$ ) (**Figure 2A**). Nearly all the background POC was found in suspended particles, whose contribution to the total POC was on average  $88 \pm 9\%$ . In respect to outliers, in five out of 29 MSC deployments, the measured POC of either suspended or sinking particle fractions was at least twice higher than POC concentrations measured at other stations in the same depth layer (**Table S5**).

Patterns of PON (**Figure S2**) were similar to those of POC, with molar POC-to-PON ratios of the suspended fraction on average slightly higher than the Redfield ratio of 6.6 (average:  $7.9 \pm 3.9$ ). The molar POC-to-PON ratios did not show any trend with depth ( $R^2 = 0.06$ ,  $p = 0.25$ ,  $n = 24$ ) and were in general agreement with molar POC-to-PON ratios measured during the EXPORTS field campaign (Graff et al., in review). Molar POC-to-PON for sinking particles varied between 3 and 16 (average:  $7.2 \pm 3.8$ ) and did not show any significant trend with depth ( $R^2 = 0.11$ ,  $p = 0.1$ ,  $n = 26$ ).

PIC was below detection in 20% of the suspended particle fractions, and in 60% of sinking particle fractions analyzed. Suspended PIC concentrations increased significantly with depth ( $R^2 = 0.40$ ,  $p = 0.05$ ,  $n = 10$ ) (**Figure 2B**). Background sinking PIC was on average  $0.4 \pm 0.3 \mu\text{g C L}^{-1}$  and remained constant with depth ( $R^2 = 0.05$ ,  $p = 0.59$ ,  $n = 8$ ). Background molar PIC-to-POC ratios calculated for suspended particles increased significantly with depth ( $R^2 = 0.80$ ,  $p < 0.001$ ,  $n = 10$ ) and were significantly higher than PIC-to-POC ratios of sinking particles in the mesopelagic (paired t-test,  $p = 0.01$ ,  $n = 5$ ) (**Figure 3A**).

Background suspended and sinking bSi concentrations and their contribution to total bSi concentrations

did not significantly change with depth between 50 and 500 m ( $R^2 = 0.06\text{--}0.18$ ,  $p = 0.17\text{--}0.49$ ,  $n = 8\text{--}11$ ) (**Figure 2C**). Suspended particles stored on average  $83 \pm 9\%$  of the total background bSi pool. Molar bSi-to-POC ratios associated with background suspended particles increased significantly with depth between 50 and 500 m ( $R^2 = 0.84$ ,  $p < 0.001$ ,  $n = 8$ ), whereas ratios of sinking particles remained constant ( $R^2 = 0.16$ ,  $p = 0.32$ ,  $n = 8$ ). Furthermore, molar bSi-to-POC ratios of sinking particles were on average higher than the ratios associated with suspended particles above 95 m ( $n = 3$ ), and lower between 350 and 500 m ( $n = 4$ ). Ratios above and below 95 m were statistically different (paired t-test,  $p = 0.01$  and  $p = 0.008$ , respectively) (**Figure 3B**).

Suspended and sinking lSi concentrations and relative contribution to the total lSi pool did not display a significant trend with depth and showed high variability ( $R^2 = 0.004\text{--}0.07$ ,  $p = 0.39\text{--}0.85$ ,  $n = 11\text{--}13$ ) (**Figure 2D**). Suspended lSi accounted, on average, for  $83 \pm 19\%$  of the total lSi pool. Molar lSi-to-POC ratios associated with suspended particles increased significantly with depth between 50 and 350 m depth ( $R^2 = 0.78$ ,  $p = 0.02$ ,  $n = 6$ ). For sinking particles, molar lSi-to-POC ratios displayed the tendency of decreasing with depth between 60 and 500 m, although the trend was not statistically significant ( $R^2 = 0.05$ ,  $p = 0.58$ ,  $n = 9$ ) (**Figure 3C**). Ratios between suspended and sinking particles were statistically different below the euphotic zone (paired t-test,  $p < 0.01$ ) with suspended particles characterized by consistently higher ratios than sinking particles.

Suspended TEP decreased significantly with depth ( $R^2 = 0.53$ ,  $p = 0.001$ ,  $n = 16$ ) and like POC, displayed the sharpest decrease between 50 and 95 m. On average,  $95 \pm 4\%$  of TEP was suspended, and sinking TEP was often at or near detection (average =  $0.3 \pm 0.2 \mu\text{g GXeq L}^{-1}$ ,  $n = 15$ ) (**Figure 2E**). TEP concentrations measured in the MSCs were in line with the concentrations measured in the water collected with the CTD rosette (**Figure S3**). After converting TEP to carbon concentration of TEP, we estimated, in 11 out of 15 deployments, that  $15 \pm 5\%$  of suspended POC was TEP and only  $3 \pm 1\%$  of sinking POC was TEP. In 4 observations collected above 100 m, TEP-C accounted for 13% of the sinking POC (**Figure 3D**). TEP-C-to-POC ratios associated with suspended and sinking particles were statistically different (paired t-test,  $p < 0.001$ ,  $n = 15$ ).

Background POC, TEP, bSi and lSi concentrations in the suspended and sinking particle pools did not display a significant variability over time at 50–65 m, 95 m or 300–500 m (t-test, 95% confidence). Temporal trend for PIC could not be tested owing to the limited number of observations available.

To provide an overall assessment of the relative changes in the measured biogeochemical composition of suspended and sinking particles with depth, we summed the background cruise-wide averaged concentrations of organic TEP-C, POC and PON and ballast minerals and evaluated the differences in their relative contributions (**Figure 4**). We found that the composition of suspended particles was dominated by POC (64%) in the euphotic zone and by POC ( $34 \pm 11\%$ ), lSi ( $30 \pm 7\%$ ) and PIC ( $16 \pm 8\%$ ) in the upper mesopelagic, whereas sinking particles were on average composed mainly by POC ( $50 \pm 10\%$ ), followed by lSi ( $20 \pm 7\%$ ), bSi ( $14 \pm 7\%$ ) and PON ( $9 \pm 3\%$ ) throughout the water column. The relative contribution of TEP-C in suspended particles was on average twice the one in sinking particles (**Figure 4B**).

### 3.4 Constraining the particle sinking velocity

The settling time experiments found no consistent differences in the fraction of sinking particles to the whole particle population (suspended plus sinking) as a function of settling time (t-test, 95% confidence). After 1, 2 and 4 hours of settling, sinking POC made up 10, 11 and 10% and sinking PON 6, 7 and 8% of the whole particle population (**Table S6**). Sinking bSi made up 23, 25 and 25%, whereas sinking TEP made up 6, 3 and 5%. However, our experiment was limited to only two casts within the euphotic zone; hence, we cannot assume that all sinking particles collected had the potential to sink within one hour at  $36 \text{ m d}^{-1}$ . We therefore present fluxes calculated assuming the standard sinking velocity of  $18 \text{ m d}^{-1}$ , and we reinforce that these fluxes represent a lower bound as suggested by our settling time experiments (**Figure 5**). Background POC fluxes averaged to  $4.2 \pm 2.6$ ,  $3.1 \pm 1.5$  and  $3.1 \pm 1.1 \text{ mmol C m}^{-2} \text{ d}^{-1}$  at 50–65 m, 95 m and 300–500

m, respectively. When including the outliers, the estimates increased up to  $7 \pm 10$ ,  $9 \pm 18$  and  $4 \pm 2$  mmol C  $\text{m}^{-2} \text{d}^{-1}$ , at these same depth intervals. Fluxes of bSi were on average 0.2, 0.2 and 0.1 mmol Si  $\text{m}^{-2} \text{d}^{-1}$  and lSi fluxes were 0.3, 0.4 and 0.2 mmol Si  $\text{m}^{-2} \text{d}^{-1}$  at 50–65 m, 95 m and 300–500 m, respectively.

## 4. Discussion

In this discussion, we first put our results into the overall cruise context and then focus on the causes that drive the differences between the suspended and sinking particles as measured with the MSC. Specifically, we discuss why – despite all particles being small – some particles sank while others remained suspended. Furthermore, we discuss the potential mechanisms that can explain the presence of small, slow sinking particles in the mesopelagic. We finally address two aspects of the methodology: (1) comparison of sinking particle fluxes derived from different methods, and (2) interpretation and implications of the observed outliers in our data set including the potential role of ‘patchiness’ on ocean particle distributions.

### 4.1 Comparison with other particulate biochemical measurements performed during EXPORTS: consistency in responses by size

A variety of methods and sampling equipment were used to measure the biogeochemical composition of particulate matter during the first EXPORTS field campaign (Siegel et al., 2021). Values of POC and PON measured in the MSC time zero fraction were slightly higher than those obtained from the 12-L Niskin bottles sampled from the CTD/rosette system from the same ship (Graff et al., in review). The differences between the two measurements may be explained by a combination of the following: (1) under sampling of sinking particles by Niskin bottles compared to the MSC, (2) slight overestimation of MSC POC values due to a possibly higher POC blank than the one used to correct the measured POC masses (see section 2.4), and (3) spatiotemporal differences in sampling (Graff et al., in review).

Our PIC concentrations were low, but consistent with low productivity regimes in the global ocean (Mitchell et al., 2017) and complimentary measurements made at Station P during EXPORTS (Roca-Martí et al., 2021), suggesting a limited presence of calcifying microorganisms. In situ pump observations showed low PIC concentrations and small contributions to particle stocks during EXPORTS (Roca-Martí et al., 2021). Our PIC estimates were higher than the in situ pump observations, which may be attributed to the use of larger filter pore size with in situ pumps (QMA;  $\sim 1.0 \mu\text{m}$  nominal pore size) compared to the smaller pore size of glass fiber filters used with Niskin bottles and MSC analyses (GF/F;  $\sim 0.3 \mu\text{m}$  nominal pore size after combustion, Nayar and Chou, 2003) (Graff et al., in review). Indeed, during EXPORTS, most of the PIC was associated with the smallest size particle fraction measured by in situ pumps (i.e., in 1–5  $\mu\text{m}$  fraction rather than in the 5–51  $\mu\text{m}$  or  $> 51 \mu\text{m}$  fractions; Roca-Martí et al., 2021).

Our measurements of bSi standing stocks were in good agreement with measurements performed on seawater collected with Niskin bottles (Brzezinski et al., 2022) and measurements obtained with in situ pumps (Roca-Martí et al., 2021), which used similar pore sizes (0.6, 0.6 and 0.8  $\mu\text{m}$ , respectively). Our molar bSi-to-POC ratios associated with suspended and sinking particles were in the same range as the 1–51  $\mu\text{m}$  particle size fractions (bSi:POC = 0.03–0.16, Roca-Martí et al., 2021), except for one outlier (0.35 at 500 m; see Section 4.5). Molar bSi-to-POC ratios measured from larger sized particles with in situ pumps and drifting sediment traps were higher (Roca-Martí et al., 2021; Estapa et al., 2021). This comparison suggests that the MSC sampled on average small particles ( $< 51 \mu\text{m}$ ), under-sampled large particles, and that using GF/F filters allowed us to better represent particles  $< 1 \mu\text{m}$  in respect to in situ pumps. Overall, the concentrations and flux values (see also section 4.4) obtained by the MSCs agreed with other measurements obtained during the cruise, and we are therefore confident that the MSC observations are representative of the conditions present in situ during our visit.

## 4.2 Partitioning of TEP and ballast minerals in suspended and sinking particles

When comparing sinking to suspended particles, we expected to find either larger particles in the sinking fraction compared with the suspended fraction, and/or a higher ratio of ballast materials-to-POC. However, neither expectation was met (**Figure. 1, 3 and 4**). Both fractions were characterized by small particles, which - in a simplistic view - would suggest that sinking particles contained a higher fraction of ballast material than suspended particles. Contrary to this idea, however, suspended particles were characterized by a higher ratio of ballast material in the mesopelagic. This begs the question why the small non-ballasted particles sank (and, why the ballasted particles did not sink).

The partitioning of particles into suspended and sinking pools must have been controlled by another factor. So far, we looked at the composition in context of the traditional constituents: POC, PIC and silicate. However, the molecular makeup of POC can have a large effect on particle density. For example, diatoms have been shown to be positively buoyant (i.e., float) (Villareal, 1988; Moore et al., 1996; Woods et al., 2008). However, the phytoplankton community consisted predominantly of very small non-diatom cells (McNair et al., 2021). Alternatively, TEP are positively buoyant and thus could reduce the sinking velocity of aggregates (Engel and Schartau, 1999; Azetsu-Scott and Passow, 2004). Overall, we observed low concentrations of water column TEP between 5 and 500 m ( $17.3\text{--}1.2 \mu\text{g GXeq L}^{-1}$ ). This result is in line with low productivity systems such as the Southern Ocean (from undetectable values to  $48 \mu\text{g GXeq L}^{-1}$ ; Ortega-Retuerta et al., 2009), the tropical western Pacific Ocean ( $5.3\text{--}40 \mu\text{g GXeq L}^{-1}$ ; Yamada et al., 2017), the Eastern Mediterranean Sea ( $5.7\text{--}25.1 \mu\text{g GXeq L}^{-1}$ ; Ortega-Retuerta et al., 2019) and the Indian and the subtropical South West Pacific ( $< 20 \mu\text{g GXeq L}^{-1}$ , Engel et al., 2020). Despite the observed low TEP concentrations, TEP-C accounted for approx. 15% of the suspended POC pool. According to theoretical calculations, a 1-mm aggregate composed solely of TEP and diatoms can sink only if less than 5% of its carbon content consists of TEP (Mari et al., 2017). Here we show that the relative contribution of TEP-C was on average three times that threshold (15%) in suspended particles while in sinking particles on average only 3% of the POC was TEP. While the model used diatom as primary particle pool, in our case most of the suspended particle pool consisted of very small cells (*Synechococcus* spp, picoeukaryotes and nanoeukaryotes; McNair et al., 2021), and possibly fragments of old cells, minerals, and detritus. Nonetheless, our data support the model implication (Mari et al., 2017) and provide evidence that the chemical composition of particulate organic carbon, and especially the contribution of exudates, is critical to understand particle sinking velocity.

Hence, the higher TEP-to-POC ratio in suspended particles compared to sinking particles may have led to the difference in the partitioning of the two particle fractions as collected by the MSC by reducing the sinking velocity of small, ballasted particles that - in the absence of TEP - would have been part of the collected sinking fraction. Whereas the suspended POC was associated with ballasting material and consisted of a large fraction of TEP, the sinking POC consisted of relatively small fractions of ballasting material and TEP. This result suggests that the ratio of ballasting material-to-POC cannot be used as a sole predictor for sinking velocity, but that organic carbon composition needs to be considered.

The importance of TEP for potentially reducing sinking velocity and thus flux was first suggested by Mari et al. (2017), and here we present the first in situ measurements suggesting that high TEP concentrations reduce particle sinking velocities. Yet, our observations are limited to one field campaign only, and hence we cannot generalize. We observed this phenomenon in a low productivity system where particle concentrations were low and TEP concentrations were high. Our dataset was collected during late summer, when the system was characterized by low concentrations of chlorophyll *a*, nutrients, particles, and ballast minerals (Siegel et al., 2021; Roca-Martí et al., 2021; Brzezinski et al., 2022). The TEP-to-particle ratio may have been higher compared to other seasons, due to stressful conditions for phytoplankton growth and high light levels (Ortega-Retuerta et al. 2009), implying that the observed mechanisms could be seasonal (Mari et al., 2017). Regardless, our data suggests that future biological pump studies should characterize POC composition, including TEP, to help gain a mechanistic understanding of how these materials influence particle sinking velocities and, in turn, the role of particle dynamics in ocean biogeochemical cycles across different productivity systems and seasons.

### 4.3 Potential mechanisms explaining small particles at depth

Our observations suggest that suspended particles were increasingly reworked with depth, e.g., a larger fraction of POC was remineralized with depth, leading to the relative increase in the ratio between ballasting material and POC with depth. Sinking POC did not decrease with depth, suggesting that either the attenuation of the sinking particle population was negligible, or an input of sinking material balanced the expected losses. If we assume that sinking particles collected at 500 m were produced at 30 m (within the mixed layer) and sank at  $18 \text{ m d}^{-1}$ , those particles would require 26 days to reach 500 m. We can estimate the loss rate assuming a temperature-dependent remineralization rate of  $0.04 \text{ d}^{-1}$  measured experimentally using a temperature of  $7 \text{ }^\circ\text{C}$  (average temperature between 30 and 500 m from CTD) and a  $Q_{10}$  of 3.5 (Iversen and Ploug, 2013; Giering et al., 2017). If particles were to sink undisturbed, 30% of the POC would have been remineralized by bacteria during that time window (26 days). Yet, such decrease was not observed.

One theoretical explanation for a lack of flux attenuation of sinking particles would be rapid physical transport processes (Omand et al., 2015; Giering et al., 2016; Siegel et al., 2023). Particle subduction or convective mixing can, however, be excluded as during our visit density stratification beneath the mixed layer was strong and consistent and lateral density gradients were weak (Siegel et al., 2021).

Alternatively, an input of sinking particles at depth may have balanced their loss. Large sinking phytodetrital aggregates were rare, implying that disaggregation of sinking aggregates was not the prevailing source of small sinking particles. However, if suspended POC existed as loosely packed aggregates within a buoyant TEP matrix (e.g., low-density aggregates; Mari et al., 2017), their disaggregation would allow dense components to sink, albeit at a relatively slow velocity. Such disaggregation could be caused by zooplankton (Passow and Alldredge, 1999) or by microbially mediated degradation processes (Passow, 2002). During microbially mediated degradation, lighter C-components may be consumed preferentially, leaving denser and more recalcitrant material in the sinking fraction (Hamanaka et al., 2002). In fact, extracellular particulate carbohydrates released by phytoplankton (i.e., TEP) are remineralized by bacteria at a faster rate than non-TEP carbon (i.e.,  $0.53$  and  $0.21 \text{ d}^{-1}$ , respectively; Harvey et al., 1995; Mari et al., 2017).

Particle flux was, in fact, dominated by fecal pellets during EXPORTS ( $\sim 80\%$ ; Durkin et al., 2021; Steinberg et al., 2023). Specifically, mini-pellets ( $\text{ESD} < 100 \text{ }\mu\text{m}$ ) contributed up to 46% of the total carbon flux in the upper mesopelagic (Durkin et al., 2021), with mesozooplankton and salp pellets contributing the majority of the sinking flux (Durkin et al., 2021; McNair et al., 2023). Fragmentation of fecal pellets, e.g., due to sloppy feeding or swimming motions (Steinberg and Landry, 2017) could have produced small and dense particles, which may have constituted the bulk of the small sinking particle pool we collected. Such pellet fragments would likely contain a high percentage of organic carbon and a low percentage of TEP, similar to our sinking particle pool. Though we did not observe large fast sinking pellets in the MSCs, this absence could have been caused by an overall low abundance of pellets or because the MSCs were deployed during the daytime when a large fraction of the zooplankton community likely resided at depth (e.g., Steinberg et al., 2023).

Microzooplankton grazing of suspended POC, and the resulting production of mini-pellets (Stemmann et al., 2004), may have also contributed to the production of small, dense sinking particles. Consumption of small particles by zooplankton and incorporation of their carbon and biogenic silica into sinking particles (Dagg et al., 2003) is especially important for carbon flux if it occurs within relatively short-path food webs (Richardson, 2019). This mechanism could also have been important during our study: Compound-specific isotope analysis (CSIA-AA) performed during our field campaign (Connor Shea, 2023, pers. commun.) found that the mesopelagic zooplankton food web at Station P was mainly (72–96 %) based on small particles ( $< 6 \text{ }\mu\text{m}$ ).

Although we cannot say with certainty why sinking flux of POC did not decrease with depth, likely a series of biologically mediated aggregation or fragmentation processes led to a replenishment of the small sinking particle pool with depth. The described mechanisms are potentially significant contributors in dictating the efficiency of the biological carbon pump, especially in stable low-productivity systems, characterized by small particles in low concentrations.

## 4.4 Comparison of fluxes derived from different methods during EXPORTS

Our background POC fluxes compared to the cruise mean POC fluxes obtained using both neutrally buoyant and surface-tethered sediment traps (Estapa et al., 2021) and water column Thorium-234 assessment (Buesseler et al., 2020) were similar in the upper 100 m, but larger below 100 m (**Figure 6**). These differences between the estimates for depths  $> 100$  m existed even when the lower-bound estimate (assuming a sinking velocity of  $18 \text{ m d}^{-1}$ ; Section 3.4) was used. In contrast, bSi flux estimates obtained from the MSC were in good agreement with those derived from the traps, but lower than the Thorium-234-based values (Roca-Martí et al., 2021) (**Figure 6**).

These three approaches for determining sinking particle fluxes differ in the design, spatiotemporal resolutions, and size of collected particles; thus, may not be directly comparable and comparisons should be made cautiously. The approaches mainly diverge in: (1) Temporal coverage: the MSC provided virtually instantaneous estimates, whereas drifting sediments trap (Gardner, 1977) and water column Thorium-234 carbon flux determinations (Buesseler et al., 1992) integrate over periods of 3–6 days (time to collect sinking particles) and 24 days (the half-life of  $^{234}\text{Th}$ ), respectively. (2) Spatial coverage: the MSC deployments have the smallest spatial resolution among these methods with 39 discrete deployments as each MSC deployment assesses the flux from a single  $\sim 100$  L sample. Drifting sediment traps sampled sinking particles from an area of  $[?] 10 \text{ km}^2$  (Siegel et al., 2008). Due to the long integration times and abundance of samples (nearly 1000),  $^{234}\text{Th}$  particle fluxes average over even larger spatial scales. (3) Minimum size of collected particles: differences in pore sizes of filters can lead to differences in measured biogeochemical concentrations. Here we measured POC using filters with a pore size of  $\sim 0.3 \mu\text{m}$ , while POC from sediment traps (Estapa et al., 2021) and water column Thorium-234 samples (Buesseler et al., 2020) were determined using filters with a pore size of  $\sim 1 \mu\text{m}$ . The filter pore sizes used to estimate bSi were  $0.6 \mu\text{m}$ ,  $\sim 1 \mu\text{m}$  and  $0.8 \mu\text{m}$  for MSC, sediment traps and Thorium-234, respectively. Additionally, drifting sediment traps often underestimate small particles due to hydrodynamics (Buesseler et al., 2007). (4) Maximum size of collected particles: the MSC likely under samples rare particles, such as large particles, as it collects a limited amount of seawater. During EXPORTS, sediment trap samples were highly impacted by zooplankton “swimmers” and fluxes were corrected to account for the removed biomass (Estapa et al., 2021).

The potential sources of discrepancies between fluxes measured from sediment traps and water column Thorium-234 were addressed in Estapa et al. (2021). Briefly, Thorium-234 fluxes measured in sediment traps were roughly three-fold smaller than water column Thorium-234 fluxes. The different temporal coverages did not play a major role due to the stability in production and exports before the EXPORTS cruise (McNair et al., 2023). The mismatch was largely attributed to under-sampling of both small particles ( $< 32 \mu\text{m}$ ) due hydrodynamic biases and rare, large particles ( $> 1 \text{ mm}$ ) and zooplankton active migrant flux by the sediment traps (Estapa et al., 2021). The size of particles collected in the polyacrylamide gel traps, which ranged from  $75$  to  $1461 \mu\text{m}$  (median of  $282 \mu\text{m}$ ), supported this hypothesis (Estapa et al., 2021). Estimates from the MSC account for the contribution of those small particles close to  $\sim 0.3 \mu\text{m}$ . Thus, the discrepancy between MSC and sediment traps may be partially explained by an under-characterization of very small ( $< 1 \mu\text{m}$ ) particles by the traps. This statement is also valid when comparing Thorium-234-based POC fluxes if we consider the pore size of the filters used and that Thorium-based fluxes were estimated assuming the POC/Th ratio of mid-sized particles ( $5\text{--}51 \mu\text{m}$ ) (Buesseler et al., 2020).

However, the MSCs did not capture large, rare particles such as aggregates, salp fecal pellets nor the active flux due to migration. We would therefore have expected to see the opposite trend: higher flux measured using Thorium-234 and traps, if large, rare particles played an important role in overall flux at the site. This comparison suggests that POC flux from the MSCs is complementary to those measured from Thorium-234 and traps. Most importantly, it suggests that small sinking particles were a relevant part of the sinking POC flux in the upper mesopelagic zone, likely exceeding the contribution of rare, large sinking particles. The fact that the MSCs and sediment traps produced similar estimates of bSi fluxes reinforced our finding that the population of sinking particles collected by the MSCs included small sinking POC missed by the other methods, whereas bSi, which was mostly associated with slightly larger particles (Roca-Martí et al., 2021;

Estapa et al., 2021; Brzezinski et al., 2022), was equally sampled by all three methods.

#### 4.5 Outliers – Patchiness or artifacts?

The dataset obtained from the MSC holds the potential of highlighting the ecosystem’s patchiness through the collection of spatially heterogeneous features. Patchiness in the ocean exists both vertically and horizontally spanning from the microscale to the mesoscale (Cassie, 1962; Siegel, 1998; Robinson et al., 2021) and is in general difficult to map with most oceanographic approaches (McNair et al., 2023). Several of our biogeochemical measurements resulted in values considerably higher than average concentrations for their collection depth (**Table S5**). These “outliers” may be attributed to patchiness or could be due to methodological artifacts. Methodological artifacts could be caused by misfiring of the MSCs at a shallower depth than intended or by contamination of the filter. The latter is improbable as replicate filters and comparisons between time zero and suspended plus sinking particle fractions would have indicated “contamination”. Additionally, filters were always visually inspected for visible particles, such as macrozooplankton, which, if present, were removed. These outliers were specific to the MSC, no outliers were detected by the 12-Liter Niskin bottles of the CTD on board *R/V Roger Revelle*.

Three of the five outliers in POC were observed on August 16, at 55 m, 95 m, 195 m, one on August 21 at 195 m, and one on September 1 at 350 m. The outlier concentrations of sinking POC measured at 55 and 95 m, which were an order of magnitude higher than any other sinking POC values, are likely reflective of in situ patchiness: the respective time zero and suspended POC concentrations were also within the upper range of the values measured at those depths. The POC measured in the time zero fraction at 55 m equals the sum of POC measured in the suspended and sinking particle fraction, confirming that the MSC samples were uncontaminated. Associated sinking PON values were also marked as outliers and the molar C-to-N ratios were reasonable (10.4 and 12.5 at 55 and 95 m, respectively), albeit somewhat higher than those of the time zero and suspended fractions (7.3 and 6.4 and 8.3 and 9.7 at 55 and 95 m, respectively). Lastly, while the associated sinking TEP were high (with the observation at 95 m being an outlier), suspended TEP concentrations agreed with TEP measured from water collected with Niskin bottles at those depths (**Figure S3**). These observations and the fact that the MSC deployment depths were chosen to specifically target “interesting” areas as seen by the CTD or UVP profiles, make us believe that the 100-L sample we collected may have included patches of unusually high biochemical concentrations.

The three POC outlier concentrations of suspended POC at 195, 195 and 350 m were associated with outlier values of PON, and could reflect POC and PON concentrations measured at 50–65 m. However, the associated suspended TEP concentrations (2.8, and 3.1  $\mu\text{g GXan equiv L}^{-1}$ ) suggest samples stemmed from below 50–65 m (**Figure S3**). Although uncertain, these too could reflect patchiness.

One value of biogenic silica (176  $\text{nmol Si L}^{-1}$ , 500 m) was more than a factor of 3 higher than the bSi measured on other days at that depth either with the Niskin bottles or the MSC (57 and 45  $\text{nmol Si L}^{-1}$ , respectively). However, associated POC concentrations were consistent with the deployment depth and the molar bSi-to-C ratio of this observation (0.35) matched the one measured for particles  $> 5 \mu\text{m}$  (bSi:POC = 0.16–0.94) collected with in situ pumps (Roca-Martí et al., 2021). Thus, we assume that this sample included a higher-than-average presence of diatoms or rhizaria. Hot spots of bSi accumulation have previously been found in low productivity systems (Crombet et al., 2010) and this depth was targeted because the UVP profile directly before the MSC deployment indicated a Rhizaria maximum. Similarly, the elevated PIC concentration associated with sinking particles (21.5  $\mu\text{g PIC L}^{-1}$ ) could potentially be attributed to the presence of foraminifera test fragments or coccoliths.

In summary, the “outliers” measured with the MSC are likely, at least in part, reflective of patchiness in concentrations of small particles in this low productivity system. Patchiness in the distribution of salp swarms was also a prevalent feature during this study (Steinberg et al., 2023). The sporadic nature of patchiness is challenging to quantify and its importance with respect to standing stocks and fluxes of an entire ecosystem hard to assess, especially in a low productivity system.

## 5. Summary and Conclusions

Small, slow sinking particles are usually under-sampled by canonical particle collection methods and thus have been poorly characterized. Hence, little is known about their origins, biogeochemical composition, and role in the ocean biogeochemical cycles.

Our study shows that suspended and sinking particles were small and similarly sized. Unexpectedly, sinking particles were not characterized by a higher contribution of ballast materials (bSi, lSi and PIC), which would have justified their sinking behavior. However, they displayed low TEP-to-POC ratios in comparison to suspended particles. This observation suggests that high TEP contribution may have increased the residence time of suspended POC and thus reduced sinking particle fluxes impacting the efficiency of the biological carbon pump. Hence, we suggest that the composition of POC (i.e., presence of gels like TEP) should be routinely measured to assess how it affects the sinking of particles.

Our data together with findings from the field campaign hypothesize that the pool of small sinking particles in the mesopelagic formed via fragmentation of sinking fecal pellets, and zooplankton-mediated repackaging of suspended particles into fecal pellets. A smaller contribution to the small sinking particulate pool may have been provided via the disaggregation of low-density suspended aggregates. Such mechanisms may be especially important in low productivity systems during late summer months.

A comparison between particle fluxes calculated from the MSC with fluxes measured with drifting sediment traps and Thorium-234, suggests that small slow sinking particles exceeded the contribution of rare, large sinking particles to POC flux in the upper mesopelagic. Our data suggests that such flux of small sinking particles tends to be underestimated by trap and Thorium approaches. Potentially this flux of small sinking particles may contribute towards resolving the budget discrepancies between sinking flux and metabolic carbon requirements in the mesopelagic (Burd et al., 2010).

## 6. References

- Allredge, AL, Silver, MW. 1988. Characteristics, dynamics and significance of marine snow. *Progress in oceanography* , 20 (1), pp.41-82. DOI: [https://doi.org/10.1016/0079-6611\(88\)90053-5](https://doi.org/10.1016/0079-6611(88)90053-5).
- Allredge, AL, Passow, U, Logan, BE. 1993. The abundance and significance of a class of large, transparent organic particles in the ocean. *Deep Sea Research Part I: Oceanographic Research Papers* ,40 (6), pp.1131-1140. DOI: [https://doi.org/10.1016/0967-0637\(93\)90129-Q](https://doi.org/10.1016/0967-0637(93)90129-Q).
- Álvarez, E, López-Urrutia, Á, Nogueira, E, Fraga, S. 2011. How to effectively sample the plankton size spectrum? A case study using FlowCAM. *Journal of plankton research* , 33 (7), pp.1119-1133. DOI: <https://doi.org/10.1093/plankt/fbr012>.
- Armstrong, RA, Lee, C, Hedges, JI, Honjo, S, Wakeham, SG. 2001. A new, mechanistic model for organic carbon fluxes in the ocean based on the quantitative association of POC with ballast minerals. *Deep Sea Research Part II: Topical Studies in Oceanography* , 49 (1-3), pp.219-236. DOI: [https://doi.org/10.1016/S0967-0645\(01\)00101-1](https://doi.org/10.1016/S0967-0645(01)00101-1).
- Azetsu-Scott, K, Passow, U. 2004. Ascending marine particles: Significance of transparent exopolymer particles (TEP) in the upper ocean. *Limnology and oceanography* , 49 (3), pp.741-748. DOI: <https://doi.org/10.4319/lo.2004.49.3.0741>.
- Baker, CA, Henson, SA, Cavan, EL, Giering, SL, Yool, A, Gehlen, M, Belcher, A, Riley, JS, Smith, HE, Sanders, R. 2017. Slow-sinking particulate organic carbon in the Atlantic Ocean: Magnitude, flux, and potential controls. *Global Biogeochemical Cycles* , 31 (7), pp.1051-1065. DOI: <https://doi.org/10.1002/2017GB005638>.
- Belcher, A, Iversen, M, Giering, S, Riou, V, Henson, SA, Berline, L, Guilloux, L, Sanders, R. 2016. Depth-resolved particle-associated microbial respiration in the northeast Atlantic. *Biogeosciences* , 13 (17), pp.4927-4943. DOI: <https://doi.org/10.5194/bg-13-4927-2016>.

- Bisson, K, Siegel, DA, DeVries, T. 2020. Diagnosing mechanisms of ocean carbon export in a satellite-based food web model. *Frontiers in Marine Science* , 7 , p.505. DOI: <https://doi.org/10.3389/fmars.2020.00505>.
- Bittar, TB, Passow, U, Hamaraty, L, Bidle, KD, Harvey, EL. 2018. An updated method for the calibration of transparent exopolymer particle measurements. *Limnology and Oceanography: Methods* , 16 (10), pp.621-628. DOI: <https://doi.org/10.1002/lom3.10268>.
- Blanco, JM, Echevarria, F, Garcia, CM. 1994. Dealing with size-spectra: some conceptual and mathematical problems. *Scientia Marina*58(1-2):17-29.
- Boyd, PW, Muggli, DL, Varela, DE, Goldblatt, RH, Chretien, R, Orians, KJ, Harrison, P.J. 1996. In vitro iron enrichment experiments in the NE subarctic Pacific. *Marine Ecology Progress Series* , 136 , pp.179-193. DOI: [10.3354/meps136179](https://doi.org/10.3354/meps136179).
- Boyd, PW, Trull, TW. 2007. Understanding the export of biogenic particles in oceanic waters: Is there consensus?. *Progress in Oceanography* , 72 (4), pp.276-312. DOI: <https://doi.org/10.1016/j.pocean.2006.10.007>.
- Boyd, PW, Claustre, H, Levy, M, Siegel, DA, Weber, T. 2019. Multi-faceted particle pumps drive carbon sequestration in the ocean. *Nature* , 568 (7752), pp.327-335. DOI: <https://doi.org/10.1038/s41586-019-1098-2>.
- Briggs, N, Dall’Olmo, G, Claustre, H. 2020. Major role of particle fragmentation in regulating biological sequestration of CO<sub>2</sub> by the oceans. *Science* , 367 (6479), pp.791-793. DOI: <https://doi.org/10.1126/science.aay179>.
- Brzezinski, MA, Varela, DE, Jenkins, BD, Buck, KN, Kafriksen, SM, Jones, JL. 2022. The upper ocean silicon cycle of the subarctic Pacific during the EXPORTS field campaign. *Elementa: Science of the Anthropocene* 10(1). DOI: <https://doi.org/10.1525/elementa.2021.00087>.
- Buesseler, KO, Antia, AN, Chen, M, Fowler, SW, Gardner, WD, Gustafsson, O, Harada, K, Michaels, AF, Rutgers van der Loeff, M, Sarin, M, Steinberg, D.K. 2007. An assessment of the use of sediment traps for estimating upper ocean particle fluxes. *Journal of Marine Research* , 65 (3), pp.345-416. DOI: <http://dx.doi.org/10.1357/002224007781567621>.
- Buesseler, KO, Benitez-Nelson, CR, Roca-Marti, M, Wyatt, AM, Resplandy, L, Clevenger, SJ, Drysdale, JA, Estapa, ML, Pike, S, Umhau, BP. 2020. High-resolution spatial and temporal measurements of particulate organic carbon flux using thorium-234 in the northeast Pacific Ocean during the EXport Processes in the Ocean from RemoTe Sensing field campaign. *Elementa: Science of the Anthropocene* , 8 (1). DOI: <https://doi.org/10.1525/elementa.2020.030>.
- Burd, AB, Hansell, DA, Steinberg, DK, Anderson, TR, Aristegui, J, Baltar, F, Beupre, SR, Buesseler, KO, DeHairs, F, Jackson, GA, Kadko, D.C. 2010. Assessing the apparent imbalance between geochemical and biochemical indicators of meso-and bathypelagic biological activity: What the @ \$! is wrong with present calculations of carbon budgets?. *Deep Sea Research Part II: Topical Studies in Oceanography* , 57 (16), pp.1557-1571. DOI: <https://doi.org/10.1016/j.dsr2.2010.02.022>.
- Cassie, RM. 1962. Frequency distribution models in the ecology of plankton and other organisms. *The Journal of Animal Ecology* , pp.65-92.
- Cavan, EL, Henson, SA, Belcher, A, Sanders, R. 2017. Role of zooplankton in determining the efficiency of the biological carbon pump. *Biogeosciences* , 14 (1), pp.177-186. DOI: <https://doi.org/10.5194/bg-14-177-2017>.
- Charette, MA, Moran, SB, Bishop, JK. 1999. <sup>234</sup>Th as a tracer of particulate organic carbon export in the subarctic northeast Pacific Ocean. *Deep Sea Res Part II* 46(11-12): 2833-2861. DOI: [https://doi.org/10.1016/S0967-0645\(99\)00085-5](https://doi.org/10.1016/S0967-0645(99)00085-5)

- Collins, JR, Edwards, BR, Thamatrakoln, K, Ossolinski, JE, DiTullio, GR, Bidle, KD, Doney, SC, Van Mooy, BA. 2015. The multiple fates of sinking particles in the North Atlantic Ocean. *Global Biogeochemical Cycles* , 29 (9), pp.1471-1494. DOI: <https://doi.org/10.1002/2014GB005037>.
- Crombet, Y, Leblanc, K, Queguiner, B, Moutin, T, Rimmelin, P, Ras, J, Claustre, H, Leblond, N, Oriol, L, Pujon-Pay, M. 2011. Deep silicon maxima in the stratified oligotrophic Mediterranean Sea. *Biogeosciences* , 8 (2), pp.459-475. DOI: <https://doi.org/10.5194/bg-8-459-2011>.
- Dagg, MJ, Urban-Rich, J, Peterson, JO. 2003. The potential contribution of fecal pellets from large copepods to the flux of biogenic silica and particulate organic carbon in the Antarctic Polar Front region near 170 W. *Deep Sea Research Part II: Topical Studies in Oceanography* , 50 (3-4), pp.675-691. DOI: [https://doi.org/10.1016/S0967-0645\(02\)00590-8](https://doi.org/10.1016/S0967-0645(02)00590-8).
- Dall’Olmo, G, Mork, KA, 2014. Carbon export by small particles in the Norwegian Sea. *Geophys. Res. Lett.*, 41, 2921-2927. DOI: <https://doi.org/10.1002/2014GL059244>.
- Dever, M, Nicholson, D, Omand, MM, Mahadevan, A. 2021. Size-differentiated export flux in different dynamical regimes in the ocean. *Global Biogeochemical Cycles* , 35 (3), p.e2020GB006764. DOI: <https://doi.org/10.1029/2020GB006764>.
- DeVries, T, Primeau, F, Deutsch, C. 2012. The sequestration efficiency of the biological pump. *Geophysical Research Letters*. 2012 Jul;39(13). DOI: <https://doi.org/10.1029/2012GL051963>.
- Durkin, CA, Estapa, ML, Buesseler, KO. 2015. Observations of carbon export by small sinking particles in the upper mesopelagic. *Marine Chemistry* , 175 , pp.72-81. DOI: <https://doi.org/10.1016/j.marchem.2015.02.011>.
- Durkin, CA, Buesseler, KO, Cetinić, I, Estapa, ML, Kelly, RP, Omand, M. 2021. A visual tour of carbon export by sinking particles. *Global Biogeochemical Cycles* , 35 (10), p.e2021GB006985. DOI: <https://doi.org/10.1029%2F2021GB006985>.
- Ebersbach, F, Trull, TW. 2008. Sinking particle properties from polyacrylamide gels during the Kerguelen Ocean and Plateau compared Study (KEOPS): Zooplankton control of carbon export in an area of persistent natural iron inputs in the Southern Ocean. *Limnology and Oceanography* , 53 (1), pp.212-224. DOI: <https://doi.org/10.4319/lo.2008.53.1.0212>.
- Engel, A, Schartau, M. 1999. Influence of transparent exopolymer particles (TEP) on sinking velocity of *Nitzschia closterium* aggregates. *Marine Ecology Progress Series* , 182 , pp.69-76. DOI: <https://www.jstor.org/stable/24852120>.
- Engel, A, Passow, U. 2001. Carbon and nitrogen content of transparent exopolymer particles (TEP) in relation to their Alcian Blue adsorption. *Marine Ecology Progress Series* , 219 , pp.1-10. DOI: <http://dx.doi.org/10.3354/meps219001>.
- Engel, A, Endres, S, Galgani, L, Schartau, M. 2020. Marvelous marine microgels: on the distribution and impact of gel-like particles in the oceanic water-column. *Frontiers in Marine Science* , 7 , p.405. DOI: <https://doi.org/10.3389/fmars.2020.00405>.
- Estapa, M, Buesseler, K, Durkin, CA, Omand, M, Benitez-Nelson, CR, Roca-Martí, M, Breves, E, Kelly, RP, Pike, S. 2021. Biogenic sinking particle fluxes and sediment trap collection efficiency at Ocean Station Papa. *Elem Sci Anth* , 9 (1), p.00122. DOI: <https://doi.org/10.1525/elementa.2020.00122>.
- Friedlingstein, P, Jones, MW, O’sullivan, M, Andrew, RM, Hauck, J, Peters, GP, Peters, W, Pongratz, J, Sitch, S, Le Quéré, C, Bakker, DC. 2019. Global carbon budget 2019. *Earth System Science Data* , 11 (4), pp.1783-1838. DOI: <https://doi.org/10.5194/essd-11-1783-2019>.
- Gardner, WD. 1977. Incomplete extraction of rapidly settling particles from water samplers 1. *Limnology and Oceanography* , 22 (4), pp.764-768. DOI: <https://doi.org/10.4319/lo.1977.22.4.0764>.

- Giering, SL, Sanders, R, Lampitt, RS, Anderson, TR, Tamburini, C, Boutrif, M, Zubkov, MV, Marsay, CM, Henson, SA, Saw, K, Cook, K. 2014. Reconciliation of the carbon budget in the ocean's twilight zone. *Nature* , 507 (7493), pp.480-483. DOI: <https://doi.org/10.1038/nature13123>.
- Giering, SLC, Sanders, R, Martin, AP, Lindemann, C, Möller, KO, Daniels, CJ, Mayor, DJ, St. John, MA. 2016. High export via small particles before the onset of the North Atlantic spring bloom. *Journal of Geophysical Research: Oceans* , 121 (9), pp.6929-6945. DOI: <https://doi.org/10.1002/2016JC012048>.
- Giering, SL, Sanders, R, Martin, AP, Henson, SA, Riley, JS, Marsay, CM, Johns, DG. 2017. Particle flux in the oceans: Challenging the steady state assumption. *Global Biogeochemical Cycles* , 31 (1), pp.159-171. DOI: <https://doi.org/10.1002/2016GB005424>.
- Giering, SL, Hosking, B, Briggs, N, Iversen, MH. 2020. The interpretation of particle size, shape, and carbon flux of marine particle images is strongly affected by the choice of particle detection algorithm. *Frontiers in Marine Science* , 7 , p.564. DOI: <https://doi.org/10.3389/fmars.2020.00564>.
- Hamanaka, J, Tanoue, E, Hama, T, Handa, N. 2002. Production and export of particulate fatty acids, carbohydrates and combined amino acids in the euphotic zone. *Marine Chemistry* , 77 (1), pp.55-69. DOI: [https://doi.org/10.1016/S0304-4203\(01\)00075-5](https://doi.org/10.1016/S0304-4203(01)00075-5).
- Harvey, HR, Tuttle, JH, Bell, JT. 1995. Kinetics of phytoplankton decay during simulated sedimentation: changes in biochemical composition and microbial activity under oxic and anoxic conditions. *Geochimica et Cosmochimica Acta* , 59 (16), pp.3367-3377. DOI: [https://doi.org/10.1016/0016-7037\(95\)00217-N](https://doi.org/10.1016/0016-7037(95)00217-N).
- Henson, SA, Sanders, R, Madsen, E, Morris, PJ, Le Moigne, F, Quartly, GD. 2011. A reduced estimate of the strength of the ocean's biological carbon pump. *Geophysical Research Letters* , 38 (4). DOI: <https://doi.org/10.1029/2011GL046735>.
- Iversen, MH, Ploug, H. 2013. Temperature effects on carbon-specific respiration rate and sinking velocity of diatom aggregates—potential implications for deep ocean export processes. *Biogeosciences* , 10 (6), pp.4073-4085. DOI: <https://doi.org/10.5194/bg-10-4073-2013>.
- Iversen, MH, Lampitt, RS. 2020. Size does not matter after all: no evidence for a size-sinking relationship for marine snow. *Progress in Oceanography* , 189 , p.102445. DOI: <https://doi.org/10.1016/j.pocean.2020.102445>.
- Iversen, MH. 2022. Carbon Export in the Ocean: A Biologist's Perspective. *Annual Review of Marine Science* , 15 . DOI: <https://doi.org/10.1146/annurev-marine-032122-035153>.
- Jackson, GA. 1995. Comparing observed changes in particle size spectra with those predicted using coagulation theory. *Deep Sea Research Part II: Topical Studies in Oceanography* , 42 (1), pp.159-184. DOI: [https://doi.org/10.1016/0967-0645\(95\)00010-N](https://doi.org/10.1016/0967-0645(95)00010-N).
- Kawakami, H, Honda, MC, Matsumoto, K, Fujiki, T, Watanabe, S. 2010. East-west distribution of POC fluxes estimated from  $^{234}\text{Th}$  in the northern North Pacific in autumn. *J Oceanogr* 66(1): 71-83. DOI: <https://doi.org/10.1007/s10872-010-0006-z>.
- Kriest, I. 2002. Different parameterizations of marine snow in a 1D-model and their influence on representation of marine snow, nitrogen budget and sedimentation. *Deep Sea Research Part I: Oceanographic Research Papers* , 49 (12), pp.2133-2162. DOI: [http://dx.doi.org/10.1016/S0967-0637\(02\)00127-9](http://dx.doi.org/10.1016/S0967-0637(02)00127-9).
- Kwon, EY, Primeau, F, Sarmiento, JL. 2009. The impact of remineralization depth on the air-sea carbon balance. *Nature Geoscience* , 2 (9), pp.630-635. DOI: <http://dx.doi.org/10.1038/ngeo612>
- Lampitt, RS, Wishner, KF, Turley, CM, Angel, MV. 1993. Marine snow studies in the Northeast Atlantic Ocean: distribution, composition and role as a food source for migrating plankton. *Marine Biology* , 116 (4), pp.689-702. DOI: <https://doi.org/10.1007/BF00355486>.

- Laurenceau-Cornec, EC, Le Moigne, FA, Gallinari, M, Moriceau, B, Toullec, J, Iversen, MH, Engel, A, De La Rocha, CL. 2020. New guidelines for the application of Stokes' models to the sinking velocity of marine aggregates. *Limnology and Oceanography* , 65 (6), pp.1264-1285. DOI: <https://doi.org/10.1002/lno.11388>.
- Mackinson, B, Moran, S, Lomas, M, Stewart, GM, Kelly, R. 2015. Estimates of micro-, nano-, and picoplankton contributions to particle export in the northeast Pacific. *Biogeosciences* 12: 3429–3446. DOI: <https://doi.org/10.5194/bg-12-3429-2015>.
- Mari, X, Passow, U, Migon, C, Burd, AB, Legendre, L. 2017. Transparent exopolymer particles: Effects on carbon cycling in the ocean. *Progress in Oceanography* , 151 , pp.13-37. DOI: <https://doi.org/10.1016/j.pocean.2016.11.002>.
- Marsay, CM, Sanders, RJ, Henson, SA, Pabortsava, K, Achterberg, EP, Lampitt, RS. 2015. Attenuation of sinking particulate organic carbon flux through the mesopelagic ocean. *Proceedings of the National Academy of Sciences* , 112 (4), pp.1089-1094. DOI: <https://doi.org/10.1073/pnas.1415311112>.
- Martin, JH, Fitzwater, SE. 1988. Iron deficiency limits phytoplankton growth in the north-east Pacific subarctic. *Nature* , 331 (6154), pp.341-343. DOI: <https://doi.org/10.1038/331341A0>.
- Meyer MG, Gong W, Kafriksen SM, Torano O, Varela DE, Santoro AE, Cassar N, Gifford S, Niebergall AK, Sharpe G, Marchetti A. (2022). Phytoplankton size-class contributions to new and regenerated production during the EXPORTS Northeast Pacific Ocean field deployment. *Elem Sci Anth* , 10 (1), 00068. DOI: <https://doi.org/10.1525/elementa.2021.00068>.
- McDonnell, AM, Buesseler, KO. 2010. Variability in the average sinking velocity of marine particles. *Limnology and Oceanography* , 55 (5), pp.2085-2096. DOI: <https://doi.org/10.4319/lo.2010.55.5.2085>.
- McNair, HM, Morison, F, Graff, JR, Rynearson, TA, Menden-Deuer, S. 2021. Microzooplankton grazing constrains pathways of carbon export in the subarctic North Pacific. *Limnology and Oceanography* , 66 (7), pp.2697-2711. DOI: <https://doi.org/10.1002/lno.11783>.
- McNair HM, Meyer MG, Lerch SJ, Maas AE, Stephens BM, Fox J, Buck KN, Burns SM, Cetinic I, Cohn MR, Durkin C. 2023. Quantitative analysis of food web dynamics in a low export ecosystem. *bioRxiv* , pp.2023-03. DOI: <https://doi.org/10.1101/2023.03.17.532807>.
- Mitchell, C, Hu, C, Bowler, B, Drapeau, D, Balch, WM. 2017. Estimating particulate inorganic carbon concentrations of the global ocean from ocean color measurements using a reflectance difference approach. *Journal of Geophysical Research: Oceans* , 122 (11), pp.8707-8720. DOI: <https://doi.org/10.1002/2017JC013146>.
- Moore, JK, Villareal, TA. 1996. Size-ascent rate relationships in positively buoyant marine diatoms. *Limnology and Oceanography* , 41 (7), pp.1514-1520. DOI: <https://doi.org/10.4319/lo.1996.41.7.1514>
- Moran, SB, Charette, MA, Pike, SM, Wicklund, CA. 1999. Differences in seawater particulate organic carbon concentration in samples collected using small- and large-volume methods: the importance of DOC adsorption to the filter blank. *Marine Chemistry* 67 (1-2): 33-42. DOI: [https://doi.org/10.1016/S0304-4203\(99\)00047-X](https://doi.org/10.1016/S0304-4203(99)00047-X).
- Nagata, T, Yamada, Y, Fukuda, H. 2021. Transparent exopolymer particles in deep oceans: synthesis and future challenges. *Gels* , 7 (3), p.75. DOI: <https://doi.org/10.3390/gels7030075>.
- Nayar, S, Chou, LM. 2003. Relative efficiencies of different filters in retaining phytoplankton for pigment and productivity studies. *Estuarine, Coastal and Shelf Science* , 58 (2), pp.241-248. DOI: [https://doi.org/10.1016/S0272-7714\(03\)00075-1](https://doi.org/10.1016/S0272-7714(03)00075-1).
- Nowicki, M, DeVries, T, Siegel, DA. 2022. Quantifying the carbon export and sequestration pathways of the ocean's biological carbon pump. *Global Biogeochemical Cycles* , 36 (3), p.e2021GB007083. DOI: <https://doi.org/10.1029/2021GB007083>.

- Obernosterer, I, Herndl, GJ. 1995. Phytoplankton extracellular release and bacterial growth: dependence on the inorganic N: P ratio. *Marine ecology progress series. Oldendorf* , 116 (1), pp.247-257. DOI: <http://dx.doi.org/10.3354/meps116247>.
- Omand, MM, D'Asaro, EA, Lee, CM, Perry, MJ, Briggs, N, Cetinić, I, Mahadevan, A. 2015. Eddy-driven subduction exports particulate organic carbon from the spring bloom. *Science* , 348 (6231), pp.222-225. DOI: <https://doi.org/10.1126/science.1260062>.
- Ortega-Retuerta, E, Reche, I, Pulido-Villena, E, Agustí, S, Duarte, CM. 2009. Uncoupled distributions of transparent exopolymer particles (TEP) and dissolved carbohydrates in the Southern Ocean. *Marine chemistry* , 115 (1-2), pp.59-65. DOI: <https://doi.org/10.1016/j.marchem.2009.06.004>.
- Ortega-Retuerta, E, Mazuecos, IP, Reche, I, Gasol, JM, Álvarez-Salgado, XA, Álvarez, M, Montero, MF, Arístegui, J. 2019. Transparent exopolymer particle (TEP) distribution and in situ prokaryotic generation across the deep Mediterranean Sea and nearby North East Atlantic Ocean. *Progress in Oceanography* , 173 , pp.180-191. DOI: <https://doi.org/10.1016/j.pocean.2019.03.002>.
- Owen, BM, Hallett, CS, Cosgrove, JJ, Tweedley, JR, Moheimani, NR. 2022. Reporting of methods for automated devices: A systematic review and recommendation for studies using FlowCam for phytoplankton. *Limnology and Oceanography: Methods* , 20 (7), pp.400-427. DOI: <https://doi.org/10.1002/lom3.10496>.
- Parekh, P, Dutkiewicz, S, Follows, MJ, Ito, T. 2006. Atmospheric carbon dioxide in a less dusty world. *Geophysical research letters* , 33 (3). DOI: <https://doi.org/10.1029/2005GL025098>.
- Passow, U. 2002. Transparent exopolymer particles (TEP) in aquatic environments. *Progress in oceanography* , 55 (3-4), pp.287-333. DOI: [https://doi.org/10.1016/S0079-6611\(02\)00138-6](https://doi.org/10.1016/S0079-6611(02)00138-6).
- Passow, U, Alldredge, AL. 1994. Distribution, size and bacterial colonization of transparent exopolymer particles (TEP) in the ocean. *Marine Ecology Progress Series* , pp.185-198. DOI: <http://dx.doi.org/10.3354/meps113185>.
- Passow, U, Alldredge, AL. 1995. A dye-binding assay for the spectrophotometric measurement of transparent exopolymer particles (TEP). *Limnology and Oceanography* , 40 (7), pp.1326-1335. DOI: <https://doi.org/10.4319/lo.1995.40.7.1326>.
- Passow, U, Alldredge, AL. 1999. Do transparent exopolymer particles (TEP) inhibit grazing by the euphausiid *Euphausia pacifica*?. *Journal of Plankton Research* , 21 (11), pp.2203-2217. DOI: <https://doi.org/10.1093/plankt/21.11.2203>.
- Passow, U. 2004. Switching perspectives: Do mineral fluxes determine particulate organic carbon fluxes or vice versa?. *Geochemistry, Geophysics, Geosystems* , 5 (4). DOI: <https://doi.org/10.1029/2003GC000670>.
- Passow, U, De La Rocha, CL. 2006. Accumulation of mineral ballast on organic aggregates. *Global Biogeochemical Cycles* , 20 (1). DOI: <https://doi.org/10.1029/2005GB002579>-
- Picheral, M, Guidi, L, Stemann, L, Karl, DM, Iddaoud, G, Gorsky, G. 2010. The Underwater Vision Profiler 5: An advanced instrument for high spatial resolution studies of particle size spectra and zooplankton. *Limnology and Oceanography: Methods* , 8 (9), pp.462-473. DOI: <https://doi.org/10.4319/lom.2010.8.462>.
- Richardson, TL. 2019. Mechanisms and pathways of small-phytoplankton export from the surface ocean. *Ann. Rev. Mar. Sci* , 11 (1), pp.57-74. DOI: <https://doi.org/10.1146/annurev-marine-121916-063627>.
- Riley, JS, Sanders, R, Marsay, C, Le Moigne, FA, Achterberg, EP, Poulton, AJ. 2012. The relative contribution of fast and slow sinking particles to ocean carbon export. *Global Biogeochemical Cycles* , 26 (1). DOI: <https://doi.org/10.1029/2011GB004085>.
- Robinson, KL, Sponaugle, S, Luo, JY, Gleiber, MR, Cowen, RK. 2021. Big or small, patchy all: Resolution of marine plankton patch structure at micro-to submesoscales for 36 taxa. *Science advances* , 7 (47), p.eabk2904.

DOI: <https://doi.org/10.1126/sciadv.abk2904>.

Roca-Martí M, Benitez-Nelson CR, Umhau BP, Wyatt AM, Clevenger SJ, Pike S, Horner TJ, Estapa ML, Resplandy L, Buesseler KO. Concentrations, ratios, and sinking fluxes of major bioelements at Ocean Station Papa. *Elem Sci Anth*. 2021 Jun 28;9(1):00166. DOI: <https://doi.org/10.1525/elementa.2020.00166>.

Siegel, DA. 1998. Resource competition in a discrete environment: Why are plankton distributions paradoxical?. *Limnology and Oceanography* , 43 (6), pp.1133-1146. DOI: <https://doi.org/10.4319/lo.1998.43.6.1133>.

Siegel DA, Fields E, Buesseler KO. 2008. A bottom-up view of the biological pump: Modeling source funnels above ocean sediment traps. *Deep Sea Research Part I: Oceanographic Research Papers* , 55 (1), pp.108-127. DOI: <https://doi.org/10.1016/j.dsr.2007.10.006>.

Siegel, DA, Buesseler, KO, Doney, SC, Sailley, SF, Behrenfeld, MJ, Boyd, PW. 2014. Global assessment of ocean carbon export by combining satellite observations and food-web models. *Global Biogeochemical Cycles* , 28 (3), pp.181-196. DOI: <https://doi.org/10.1002/2013GB004743>.

Siegel, DA, Cetinić, I, Graff, JR, Lee, CM, Nelson, N, Perry, MJ, Ramos, IS, Steinberg, DK, Buesseler, K, Hamme, R, Fassbender, AJ. 2021. An operational overview of the EXport Processes in the Ocean from RemoTe Sensing (EXPORTS) Northeast Pacific field deployment. *Elem Sci Anth* , 9 (1), p.00107. DOI: <https://doi.org/10.1525/elementa.2020.00107>.

Siegel, DA, DeVries, T, Cetinić, I, Bisson, KM. 2023, Quantifying the Ocean's Biological Pump and its Carbon Cycle Impacts on Global Scales. *Annual Review of Marine Sciences* . DOI: <https://doi.org/10.1146/annurev-marine-040722-115226>.

Sieracki, CK, Sieracki, ME, Yentsch, CS. 1998. An imaging-in-flow system for automated analysis of marine microplankton. *Marine Ecology Progress Series* , 168 , pp.285-296. DOI: <http://dx.doi.org/10.3354/meps168285>

Steinberg, D.K., Stamieszkin, K., Maas, A.E., Durkin, C.A., Passow, U., Estapa, M.L., Omand, M.M., McDonnell, A.M., Karp-Boss, L., Galbraith, M. and Siegel, D.A., 2023. The Outsized Role of Salps in Carbon Export in the Subarctic Northeast Pacific Ocean. *Global Biogeochemical Cycles* , 37 (1), p.e2022GB007523. DOI: <https://doi.org/10.1029/2022GB007523>

Steinberg, DK, Landry, MR. 2017. Zooplankton and the ocean carbon cycle. *Annual review of marine science* , 9 , pp.413-444. DOI: <https://doi.org/10.1146/annurev-marine-010814-015924>

Stemmann, L, Jackson, GA, Ianson, D. 2004. A vertical model of particle size distributions and fluxes in the midwater column that includes biological and physical processes—Part I: model formulation. *Deep Sea Research Part I: Oceanographic Research Papers* , 51 (7), pp.865-884. DOI: <http://dx.doi.org/10.1016/j.dsr.2004.03.001>.

Strickland, JDH, Parsons, TR. 1968. A practical handbook of seawater analysis fisheries. Research Board of Canada Ottawa. *Bulletin* , 167 , pp.185-206.

Tabata S, Boston NE, Boyce FM. 1965. The relation between wind speed and summer isothermal surface layer of water at ocean station P in the eastern subarctic Pacific Ocean. *Journal of Geophysical Research* , 70 (16), pp.3867-3878. DOI: <https://doi.org/10.1029/JZ070i016p03867>.

Timothy, D, Wong, C, Barwell-Clarke, J, Page, J, White, L, Macdonald, RW. 2013. Climatology of sediment flux and composition in the subarctic Northeast Pacific Ocean with biogeochemical implications. *Prog Oceanogr* 116: 95–129. DOI: <http://dx.doi.org/10.1016/j.pocean.2013.06.017>.

Villareal, TA. 1988. Positive buoyancy in the oceanic diatom *Rhizosolenia debaryana* H. Pergallo. *Deep Sea Research Part A. Oceanographic Research Papers* , 35 (6), pp.1037-1045. DOI: [https://doi.org/10.1016/0198-0149\(88\)90075-1](https://doi.org/10.1016/0198-0149(88)90075-1).

Volk, T, Hoffert, MI. 1985. Ocean carbon pumps: Analysis of relative strengths and efficiencies in ocean-driven atmospheric CO<sub>2</sub> changes. *The carbon cycle and atmospheric CO<sub>2</sub>: natural variations Archean to present* , 32 , pp.99-110. DOI: <https://doi.org/10.1029/GM032p0099>.

Wong, C, Waser, N, Whitney, F, Johnson, W, Page, J. 2002. Time-series study of the biogeochemistry of the North East subarctic Pacific: reconciliation of the Corg/N remineralization and uptake ratios with the Redfield ratios. *Deep Sea Res Part II* 49(24–25): 5717–5738. DOI: [https://doi.org/10.1016/S0967-0645\(02\)00211-4](https://doi.org/10.1016/S0967-0645(02)00211-4).

Woods, S, Villareal, TA. 2008. Intracellular ion concentrations and cell sap density in positively buoyant oceanic phytoplankton. *Nova Hedwigia Beiheft* , 133 , pp.131-145.

Yamada, Y, Yokokawa, T, Uchimiya, M, Nishino, S, Fukuda, H, Ogawa, H, Nagata, T. 2017. Transparent exopolymer particles (TEP) in the deep ocean: full-depth distribution patterns and contribution to the organic carbon pool. *Marine Ecology Progress Series* , 583 , pp.81-93. DOI: <http://dx.doi.org/10.3354/meps12339>.

## Contributions

Contributed to conception and design: UP, DAS

Contributed to acquisition of data: UP, JS, ER, SLG

Contributed to analysis and interpretation of data: ER, UP, DAS, SLG

Drafted and/or revised the article: ER, UP, DAS, SLG, JS

Approved the submitted version for publication: All

## Acknowledgements

The authors are grateful to the EXPORTS science team for the collaborative effort, data and ideas exchange and scientific production that acted as a baseline for the present work. We would like to acknowledge support from the NASA Ocean Biology and Biogeochemistry program. Thanks go to the captain and crew of the R/Vs *Revelle* and to the Ship Operations staff of the Scripps Institution of Oceanography. We also thank Stuart Halewood and Nils Haëntjens who provided support at sea and Marianne Pelletier who helped with the analysis of the silica samples. Finally, we thank Dr. Margaret Estapa, Dr. Montserrat Roca Martí and Dr. Carolina Cisternas-Novoa for their valuable feedback on the preliminary draft of the manuscript.

### Funding information

DAS, UP, ER: NASA 80NSSC17K0692

ER: Supported by the UCSB Earth Research Institute (150RE1)

### Competing interests

The authors declare no competing interests.

### Data accessibility statement

All data presented here are publicly available on the NASA data repository, SeaBASS along with all other EXPORTS data. The data can be accessed here: <https://seabass.gsfc.nasa.gov/cruise/EXPORTSNP>.

### Figures

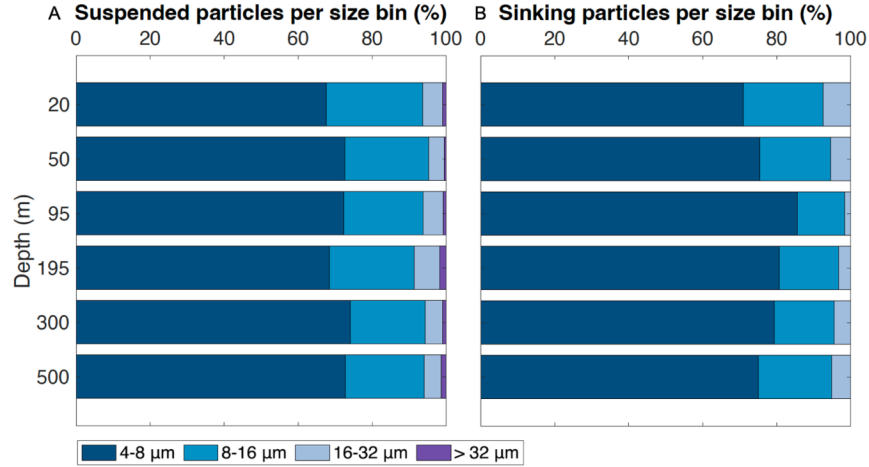
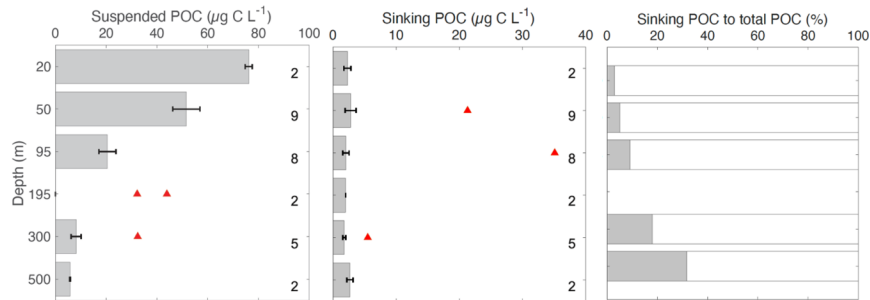


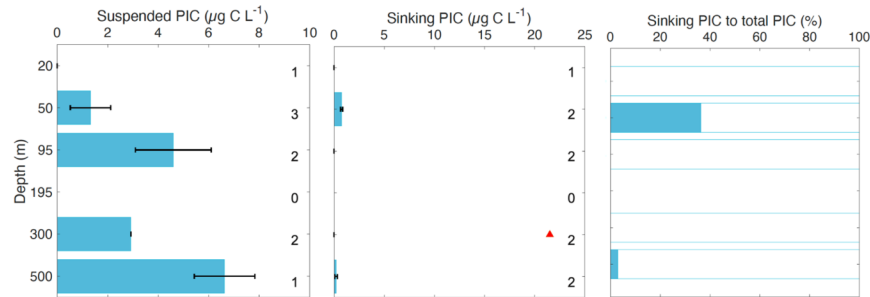
**Figure 1. Ρελατιε ζοντριβυτιον οφ παρτιςλε αβυνδανςες περ σιζε (4 το > 32 μμ) ερςυς δεπτη.**

Bar plots display the contribution in % of suspended (A) and sinking (B) particle concentrations in 4 size bins based on the octave scale (4–8, 8–16, 16–32 and > 32 μm) and on the particle equivalent spherical diameter (ESD). Concentrations are calculated as cruise-wide averages for 6 depth layers (20–25, 50–65, 95, 195, 300–350 and 500 m). Numbers of stations per depth layer are 2, 10, 10, 2, 4 and 2, respectively for bins between 4 and 32 μm and 2, 4, 5, 2, 2 and 1 for the largest size bin (> 32 μm). Sinking particles (> 32 μm) were at the detection limit of our method.

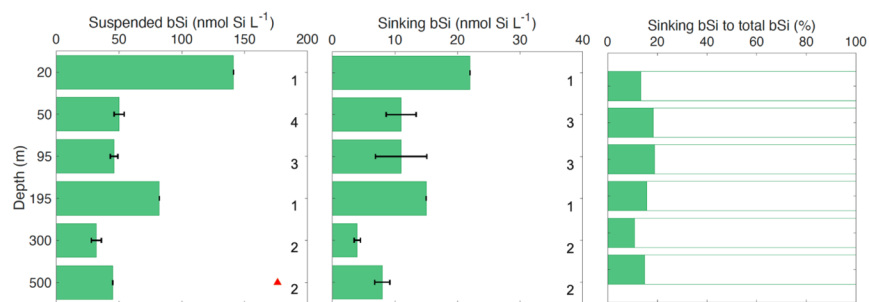
A)



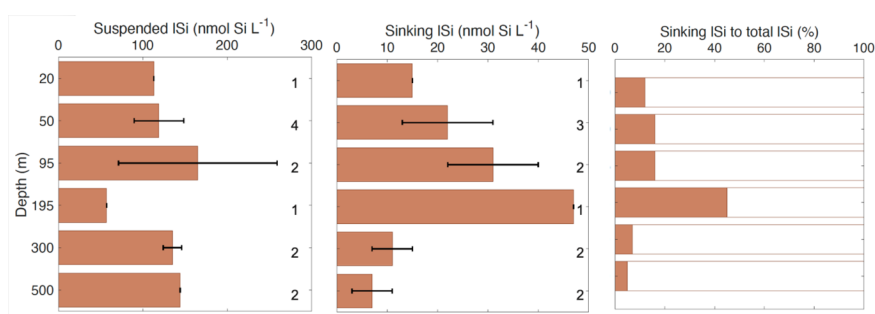
B)



C)



D)



E)

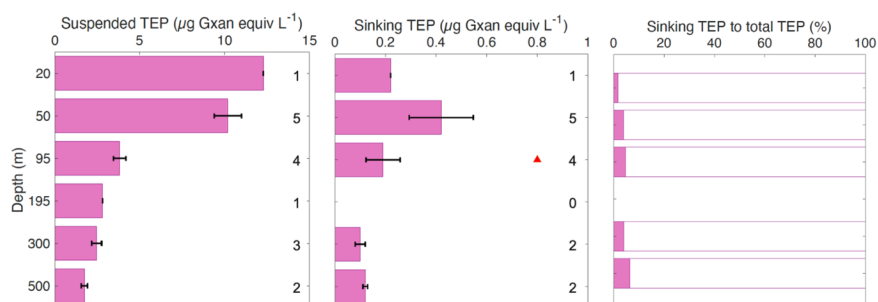


**Figure 2. Time-averaged concentrations of biogeochemical components in suspended and sinking particles and the partition of sinking particles to total.**

Bar graphs display background suspended (left) and sinking (middle) particles and the fractional contribution of sinking particle concentrations to the total (in %; right) for (A) POC, (B) PIC, (C) bSi, (D) lSi, (E) TEP concentrations. Outliers are represented as red triangles. The values are cruise-wide averages calculated for six depth layers (20–25, 50–65, 95, 195, 300–350 and 500 m). Error bars are the standard deviations of the concentrations averaged within each depth layer and thus are reflective of the dataset variability rather than the propagated uncertainty of each datapoint. Numbers on the right of each bar plot are representative of the total number of observations per depth layer. Note that the differences in the number of observations between sinking and suspended particles is reflective of loss of samples during analysis. Note differences in scales.

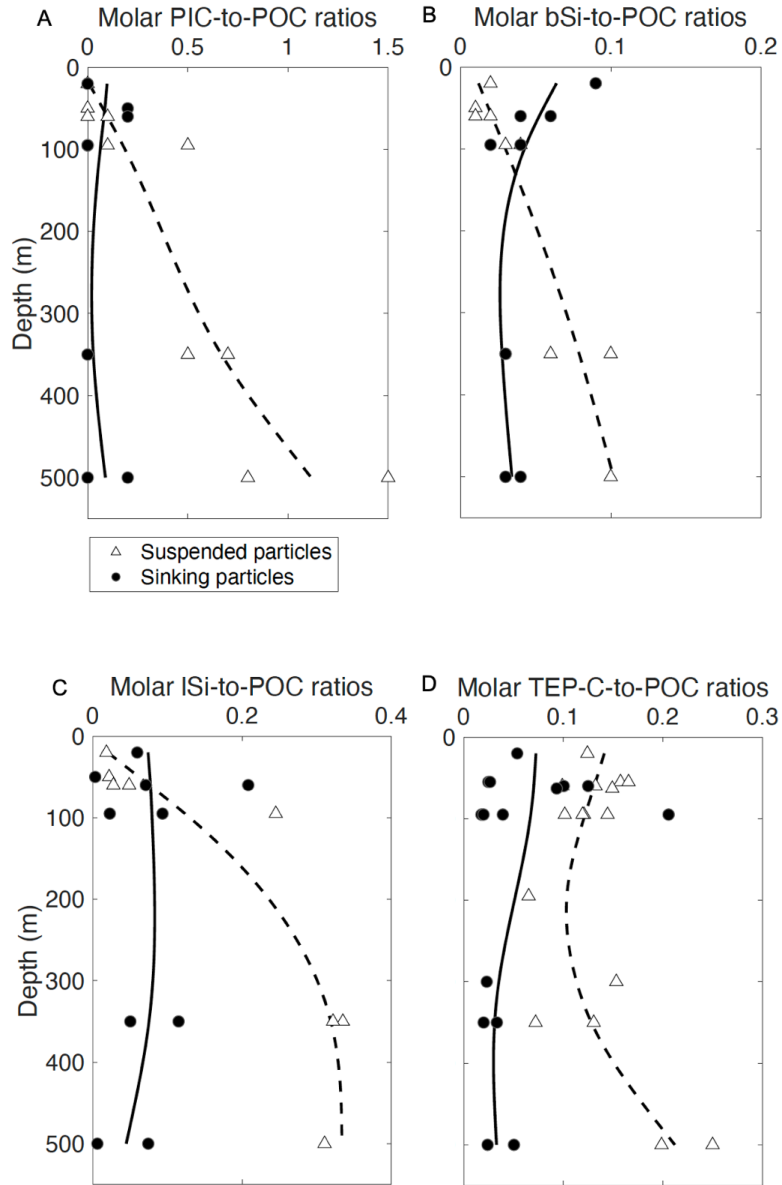
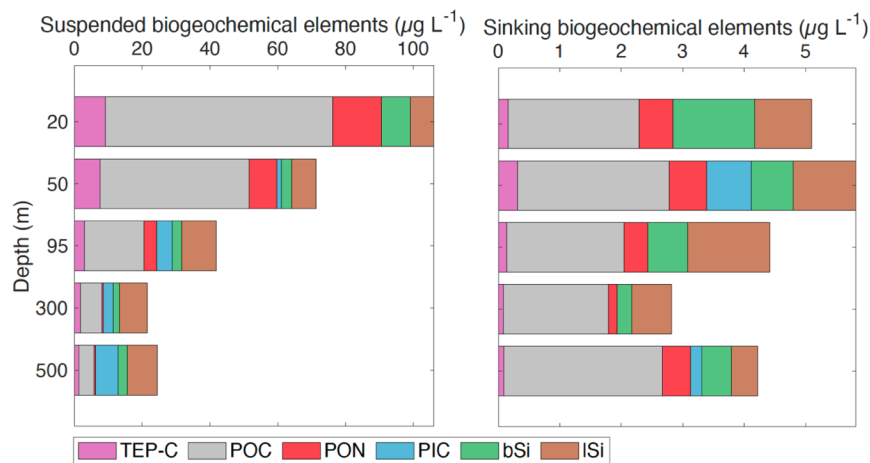


**Figure 3. Molar ratios of ballast minerals and TEP to POC in suspended and sinking particles versus depth.**

Scatter plots display the depth profile of molar PIC:POC ratios (A), molar bSi:POC ratios (B), molar lSi:POC ratios (C) and molar TEP-C:POC ratios (D) calculated for suspended (white triangles) and sinking (black circles) particles. Dash and continuous line are smoothing spline used to enhance trends visualization and thus do not have statistical significance. Outliers of suspended molar bSi-POC ratio (0.35, 500 m) and sinking PIC-to-POC ratios (12.4, 350 m) have been removed to better display depth trends, which are not affected by their exclusion.

A)



B)



**Figure 4. Concentrations of organic and inorganic elements in suspended and sinking particles and their contribution to the total measured elements.**

Bar plots display the summed biogeochemical concentrations (in  $\mu\text{g L}^{-1}$ ) (A), and their relative contributions (in %) (B) of the measured organic (TEP-C, POC, PON) and inorganic (PIC, bSi and ISi) components of suspended (left) and sinking particles (right) at five depth layers (50–65, 95, 300–350 and 500 m). Biogenic and lithogenic silica were converted to mass units using a molar mass of  $61 \text{ g mol}^{-1}$ . Here we display POC (grey) as total POC minus TEP-C. The compositional plots display background concentrations and reflect the measured particle composition.

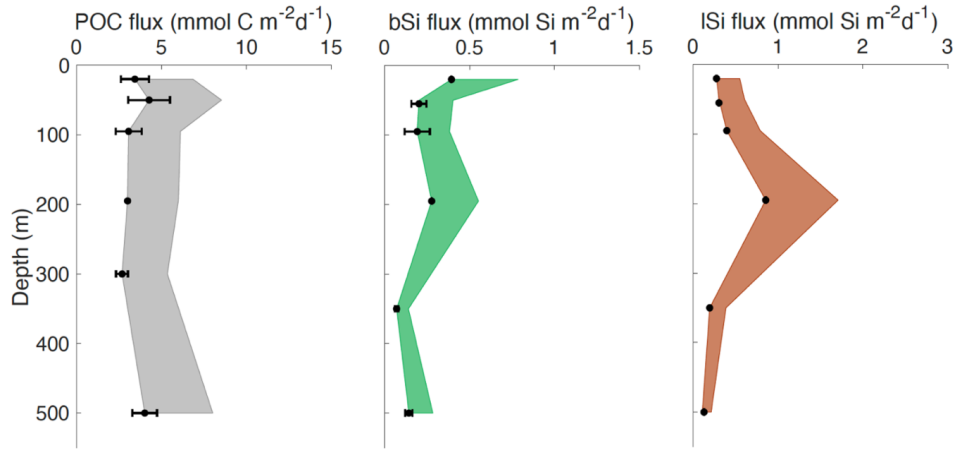


**Figure 5. Background fluxes of particulate organic carbon, biogenic and lithogenic silica versus depth.**

Plots represent fluxes of POC (grey), bSi (green) and lSi (brown) calculated using the background biogeochemical concentrations and a conservative sinking velocity of  $18 \text{ m d}^{-1}$ . The filled area represents the upper bound fluxes up to values estimated using a sinking velocity of  $36 \text{ m d}^{-1}$ . The values are cruise-wide averages calculated for five depth layers (50–65, 95, 195, 300–350 and 500 m). Error bars are calculated as standard deviations averaged within each depth layer and thus are reflective of the dataset variability rather than the propagated uncertainty of each datapoint. Note that we have one observation for all biogeochemical components at 195 m and one for bSi and lSi at 20 m. Hence, these depths are not well represented by our dataset.

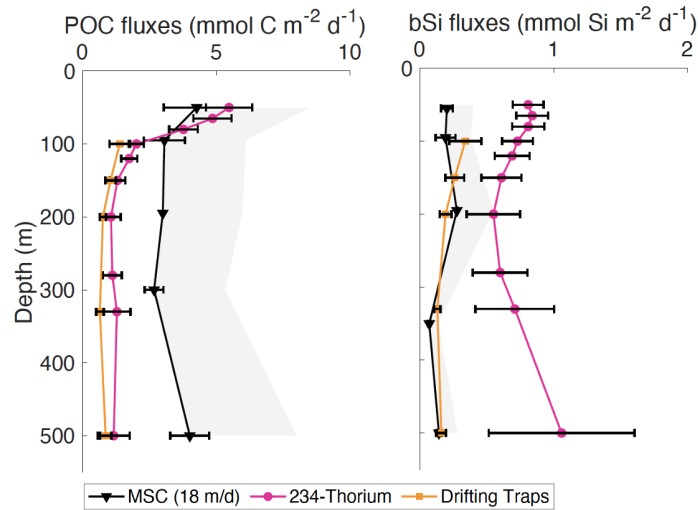


**Figure 6. Comparison of particulate organic carbon and biogenic silica fluxes estimated using different approaches during EXPORTS.**

Depth profiles of POC (left) and bSi (right) fluxes obtained from the MSC assuming a sinking velocity of  $18 \text{ m d}^{-1}$  (black triangles) to  $36 \text{ m d}^{-1}$  (filled area), Thorium-234 assessment (pink circles, Buesseler et al., 2020) and drifting sediment traps (orange squares, Estapa et al., 2021). The MSC fluxes are calculated using

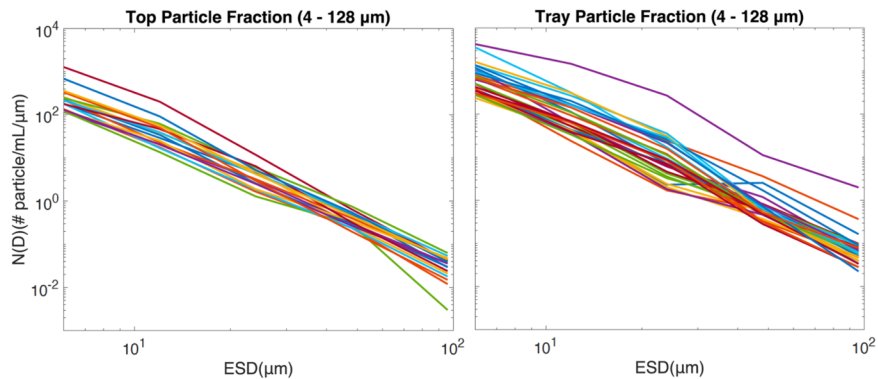
the background biogeochemical concentrations. Note that we do not consider the 195 m depth to be well represented due to there being only a single POC and bSi observation at that depth.

### Supplemental material

#### Figure S1. Particle size distribution (PSDs) of *top* and *tray* particle fractions.

Panel A shows PSDs calculated using particle concentrations of *top* and *tray* fractions with Equivalent Spherical Diameter (ESD) between 4 and 128  $\mu\text{m}$ . Panel B display PSDs slopes versus depth of *top* (white squares) and *tray* (black circles) particle fractions.

A)



B)

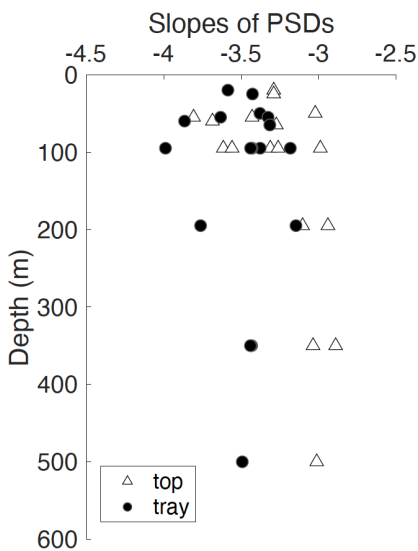


#### Figure S2. Time-averaged concentration of PON in suspended and sinking particles and the partition of sinking particles to total.

Bar graphs display background suspended (left) and sinking (middle) and the fractional contribution of sinking particle concentrations to the total (in %; right) for PON concentrations. Outliers are represented as red triangles. The values are cruise-wide averages calculated for six depth layers (20–25, 50–65, 95, 195,

300–350 and 500 m). Error bars are the standard deviations of the concentrations averaged within each depth layer and thus are reflective of the dataset variability rather than the propagated uncertainty of each datapoint. Numbers on the right are representative of the total number of observations per depth layer.

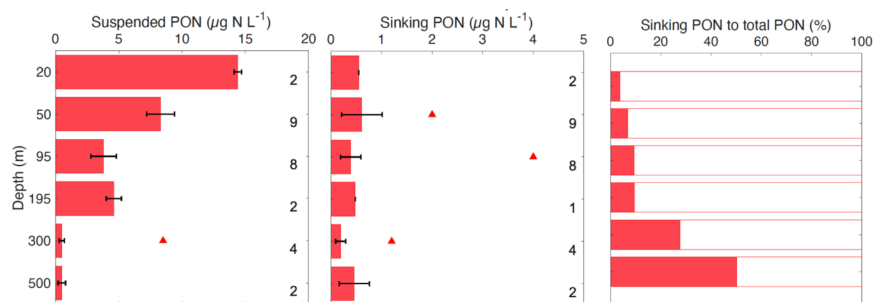


**Figure S3. Comparison of TEP concentrations measured on seawater collected with Niskin bottles and the MSCs.**

Scatter plot displays a comparison of TEP concentrations estimated in the whole water column collected with the Niskin bottles (green), by summing suspended and sinking TEP collected with the MSC (red) and in the MSC time zero fraction (lilac).

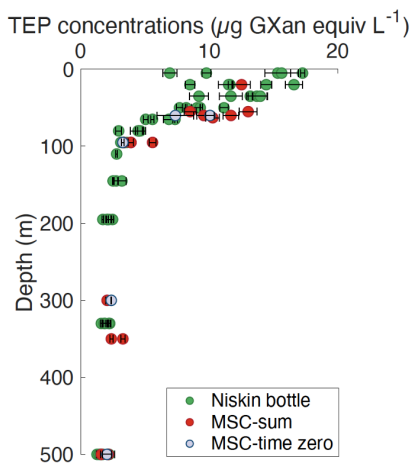


**Table S1. Summary of Marine Snow Catcher’s deployments ordinated through time.**

Table shows the type of sampling performed for each MSC deployment. The symbol - is reflective of lack of sampling.

Date in 2018 (UTC)	Epoch	Depth m	Lat °N	Lon °E	BGC measurements	FlowCam	Settling Time Test
August 16, 04:24	1	55	50.107	-145.071	POC/N, TEP	X	-
August 16, 03:56	1	95	50.107	-145.071	POC/N, TEP	X	-
August 16, 03:03	1	195	50.107	-145.071	POC/N, TEP	-	-
August 17, 23:42	1	195	50.200	-145.041	POC/N, TC, bSi/lSi	-	-
August 18, 00:44	1	55	50.200	-145.041	POC/N, TC, bSi/lSi	-	-
August 18, 00:17	1	95	50.200	-145.041	TC, bSi/lSi	X	-

August 20, 04:38	1	80	50.320	-145.073	POC/N, bSi	-	4 hours
August 20, 04:59	1	80	50.320	-145.073	POC/N, bSi, TEP	-	2 hours
August 20, 05:19	1	80	50.320	-145.073	POC/N, bSi, TEP	-	1 hour
August 20, 23:43	1	195	50.366	-145.063	POC/N	X	-
August 21, 00:48	1	65	50.366	-145.063	POC/N	X	-
August 21, 00:22	1	95	50.366	-145.063	POC/N	X	-
August 24, 01:12	2	63	50.412	-145.125	POC/N, TEP	X	-
August 24, 00:45	2	95	50.412	-145.125	POC/N, TEP	X	-
August 24, 00:08	2	350	50.412	-145.125	POC/N, TEP	X	-
August 25, 23:54	2	350	50.461	-145.005	POC/N, TC, bSi/lSi	X	-
August 26, 00:54	2	60	50.461	-145.005	POC/N, TC	X	-
August 26, 00:32	2	95	50.461	-145.005	POC/N, TC, bSi/lSi	X	-
August 28, 01:22	2	60	50.476	-144.898	POC/N, TC, TEP	X	-
August 28, 01:52	2	500	50.476	-144.898	POC/N, TC, bSi/lSi, TEP	-	-
August 29, 01:07	2	60	50.489	-144.838	POC/N, TEP	X	-
August 29, 00:44	2	95	50.489	-144.838	POC/N, TEP	X	-
August 29, 00:11	2	300	50.489	-144.838	POC/N, TEP	X	-
September 01, 03:58	3	55	50.584	-144.863	POC/N, TEP	X	-
September 01, 06:10	3	95	50.584	-144.863	POC/N, TEP	X	-
September 01, 06:41	3	350	50.584	-144.863	POC/N, TEP	X	-
September 02, 22:58	3	350	50.577	-144.748	POC/N, TC, bSi/lSi	X	-
September 03, 00:54	3	50	50.577	-144.748	POC/N, TC, bSi/lSi	X	-
September 03, 00:30	3	95	50.577	-144.748	POC/N, TC, bSi/lSi	X	-
September 05, 00:55	3	20	50.534	-144.694	POC/N, TC, bSi/lSi, TEP	X	-
September 05, 00:14	3	500	50.534	-144.694	POC/N, TC, bSi/lSi, TEP	X	-
September 05, 23:59	3	95	50.487	-144.717	POC/N	X	-
September 06, 00:48	3	25	50.487	-144.717	POC/N	X	-
September 06, 00:24	3	60	50.487	-144.717	POC/N	X	-
September 08, 19:35	3	60	50.558	-144.677	POC/N, bSi, TEP	-	4 hours
September 08, 20:04	3	60	50.558	-144.677	POC/N, bSi, TEP	-	2 hours
September 08, 20:30	3	60	50.558	-144.677	POC/N, bSi, TEP	-	1 hour

**Table S2. FlowCam technical specification and detailed methods explanation.**

Table show the protocol implemented to image and count marine particles using the FlowCam. The template we used is a modification of the template offered in Owen et al., 2022.

FlowCam technical specifications	FlowCam technical specifications
FlowCam model number	8410
FlowCam unit serial number	10446
Camera resolution	1920 x 1200 pixels
Camera	Color
Fluidics	Syringe pump (0.5 mL for 20x, 5.0 mL for 4x)
Software details	VisualSpreadsheet© software version 4.15.1

Sample details	Sample details
Preservation methods	Seawater samples preserved with 37% buffered formaldehyde to a final concentration of 1–2%
Pre-filtration details	Subsamples of the <i>base</i> and <i>tray</i> fractions were pre-filtered before analysis at 20x using a 44 µm mesh

---

<p>FlowCam setup details for analysis with the 20x objective          Flow cell sizes and types used, and objectives used for each flow cell          Calibration factor          Image acquisition mode          Flow rate          Example of full context settings for 20180816_0356_001_NSP</p>	<p>FlowCam setup details for analysis with the 20x objective          50x300 <math>\mu\text{m}</math> flow cell (FOV), 20x objective          0.3380          Auto-image          0.03 <math>\text{mL min}^{-1}</math>          Run: Mode: AutoImage Priming Method: machine prime Flow Rate: 0.030 ml/min Recalibrations: 1 Stop Reason: Sample Volume Processed Sample Volume Aspirated: 1.0000 ml Sample Volume Processed: 0.9990 ml Fluid Volume Imaged: 0.3388 ml Efficiency: 33.9% Particle Count: 1239 Images: Total: 38201 Used: 1219 Percentage Used: 3.19% Particles Per Used Image: 1.02 Particles Per Image: 0.03 Particles Per Image: 0.03 Frame Rate: 19.57 fps Intensity Mean: 177.09 Intensity Min: 174.78 Intensity Max: 177.72 Date/Time: Start: 2019-08-22 10:48:26 End: 2019-08-22 11:21:52 Sampling Time: 00:32:31 Environment: Software: VisualSpreadsheet 4.15.1 Magnification: 20X Calibration Factor: 0.3380 GumStix Firmware: 23 Calibration Factor: 0.3380 SerialNo: 10446 Number of Processors: 8 Pump: C80 Syringe Syringe Size: 0.50 ml Capture Parameters: Distance To Neighbor=30 Threshold Dark=15.0000 Threshold Light=18.0000 Close Holes=0 Capture Dark or Light Pixels=2</p>
---	---

---

<p>FlowCam setup details for analysis with the 4x objective          Flow cell sizes and types used, and objectives used for each flow cell          Calibration factor          Image acquisition mode          Flow rate</p>	<p>FlowCam setup details for analysis with the 4x objective          300x1500 <math>\mu\text{m}</math> flow cell (FOV), 4x objective          1.8130          Auto-image          0.9 <math>\text{mL min}^{-1}</math></p>
--	---

Example of full context settings for  
20180817\_2205\_001\_NSP

Run: Mode: AutoImage Priming Method: machine  
prime Flow Rate: 0.900 ml/min Recalibrations: 0  
Stop Reason: Sample Volume Processed Sample  
Volume Aspirated: 9.9892 ml Sample Volume  
Processed: 9.9544 ml Fluid Volume Imaged: 6.9242  
ml Efficiency: 34.9% Particle Count: 1542 Images:  
Total: 2648 Used: 1166 Percentage Used: 44.03%  
Particles Per Used Image: 1.32 Particles Per  
Image: 0.58 Particles Per Image: 0.58 Frame Rate:  
3.99 fps Intensity Mean: 168.49 Intensity Min:  
167.68 Intensity Max: 169.85 Date/Time: Start:  
2019-09-10 11:04:32 End: 2019-09-10 11:16:10  
Sampling Time: 00:11:03 Environment: Software:  
VisualSpreadsheet 4.15.1 Magnification: 4X  
Calibration Factor: 1.8130 GumStix Firmware: 23  
Calibration Factor: 1.8130 SerialNo: 10446  
Number of Processors: 8 Pump: C80 Syringe  
Syringe Size: 5.00 ml Capture Parameters:  
Distance To Neighbor=50 Threshold  
Dark=15.0000 Threshold Light=18.0000 Close  
Holes=0 Capture Dark or Light Pixels=2

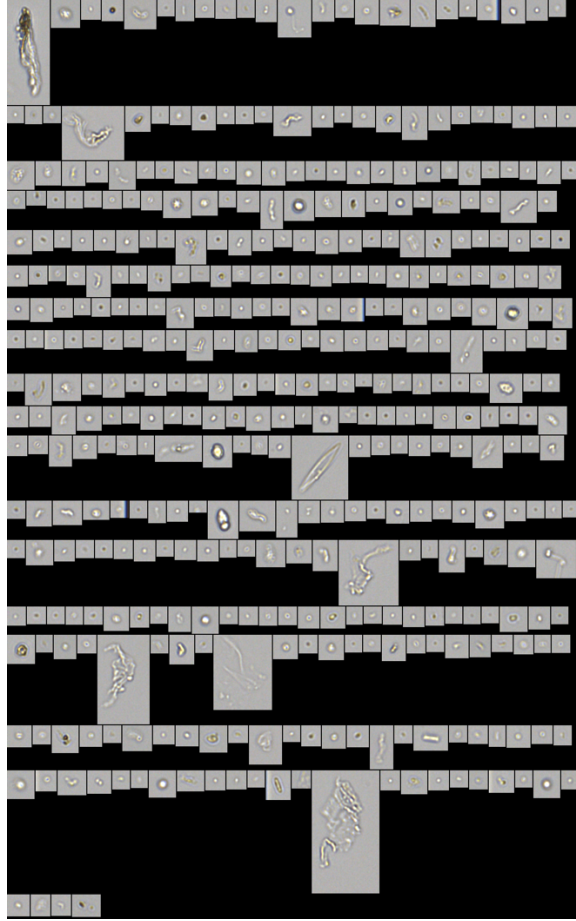
---

Measurement outputs  
Measurement type(s) used  
Justification for this choice

Measurement outputs  
Equivalent Spherical Diameter (ESD)  
Measurement type chosen based on particles type:  
particles were very small, mostly round, and  
transparent (see example of images below).  
VisualSpreadsheet© software version 4.15.1.  
identifies pixels that comprise a particle by  
distinguishing them from the image background  
taken automatically at each run. Among other  
parameters, the software estimates the Area-Based  
Diameter (hereafter ABD) and the Equivalent  
Spherical Diameter (hereafter ESD). ABD is the  
diameter calculated based on a circle with an area  
equal to the ABD area. The ABD area is  
determined by the number of dark pixels in the  
binary imaged particle, excluding inner light pixels.  
ESD is the mean value of 36 feret measurements.  
Feret measurements are the perpendicular distance  
between parallel tangents touching opposite sides  
of the particle (VisualSpreadsheet 5 Particle  
Analysis Software manual). ABD would be  
expected to underestimate the size of particles with  
internal transparent components, while ESD would  
be expected to overestimate the size of particles  
with protrusions or flagella (Owen et al., 2022).

---

Examples of suspended particles imaged at x200 (left) and x40 (right):



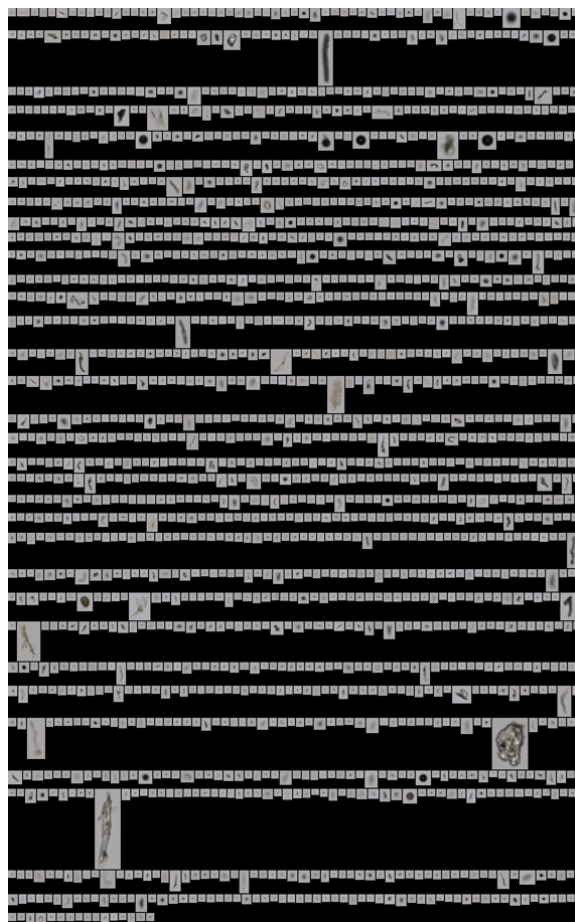


**Table S3.** Relative standard deviations ( $\sigma^2$ ) used as part of the Monte Carlo method to account for uncertainties propagation .

Biogeochemical component	$\sigma^2$ of suspended particles (%)	$\sigma^2$ of slow-sinking particles (%)	$\sigma^2$ of fast-sinking particles (%)
POC	17	6	28
PON	20	14	28
TEP	11	13	19

**Ταβλε Σ4.** Παρτιςλε ζονςεντρατιονς εστιματεδ ωιτην 5 σιζε βινς βασεδ ον παρτιςλε Εχυιαλεντ Σπηερισαλ Διαμετερς (ΕΣΔ) σπαννινγ φρομ 4 το 128 μμ.

The table shows suspended and sinking particle concentration (particles mL<sup>-1</sup>) grouped in size bins according to their equivalent spherical diameter (ESD). The abbreviation “na” is reflective of unmeasured values. Zeros are reflective of negative or null concentrations.

Date in 2018 (UTC)	Depth m	Suspended particles 4-8 μm particles mL <sup>-1</sup>	Suspended particles 8-16 μm particles mL <sup>-1</sup>	Suspended particles 16-32 μm particles mL <sup>-1</sup>	Suspended particles 32-64 μm particles mL <sup>-1</sup>	Suspended particles 64-128 μm particles mL <sup>-1</sup>
August 16, 03:56	95	741	413	251	na	na
August 16, 04:24	55	3036	1273	359	na	na
August 17, 23:42	195	720	233	71	16	2

August 18, 00:17	95	540	142	27	8	1
August 18, 00:44	55	1032	305	80	9	1
August 20, 23:43	195	469	165	50	10	2
August 21, 00:22	95	484	109	21	9	0
August 21, 00:48	65	723	136	30	8	1
August 24, 00:08	350	1025	373	151	na	na
August 24, 00:45	95	941	263	62	na	na
August 24, 01:12	63	2143	686	90	na	na
August 25, 23:54	350	1982	497	92	na	na
August 26, 00:32	95	1702	463	144	na	na
August 26, 00:54	60	528	201	44	na	na
August 28, 01:33	60	1183	298	67	na	na
August 28, 01:53	500	1344	331	71	na	na
August 29, 00:11	95	1082	238	23	na	na
August 29, 00:44	95	629	165	21	na	na
August 29, 01:07	60	2391	343	29	na	na
September 01, 03:58	55	5115	1615	190	21	3
September 01, 06:10	95	900	274	41	9	2
September 01, 06:41	350	880	183	52	13	3
September 02, 23:58	350	508	200	30	11	3
September 03, 00:30	95	521	164	40	9	2
September 03, 00:54	50	982	497	97	24	4
September 05, 00:14	500	865	316	68	17	3
September 05, 00:55	20	714	375	103	10	2
September 05, 23:59	95	2745	736	84	18	2
September 06, 00:24	60	1327	402	48	6	1
September 06, 00:48	25	1441	455	68	14	3

**Table S5. Concentrations of suspended and sinking particulate biogeochemical elements.**

Particulate organic carbon and nitrogen (POC and PON), particulate inorganic carbon (PIC), biogenic and lithogenic silica (bSi and lSi) and transparent exopolymer particles (TEP) concentrations associated with suspended (SU) and sinking (S) particles. Values in bold are the outliers discussed in paragraph 4.5. The abbreviation “na” is reflective of values that were either not collected or lost during analysis. The propagated uncertainty is denoted as “sd”.

Date in 2018 (UTC)	Depth (m)	POC ( $\mu\text{g C L}^{-1}$ ) SU	POC ( $\mu\text{g C L}^{-1}$ ) SU <sub>sd</sub>	POC ( $\mu\text{g C L}^{-1}$ ) S	POC ( $\mu\text{g C L}^{-1}$ ) S <sub>sd</sub>	PON ( $\mu\text{g N L}^{-1}$ ) SU
September 05, 00:55	20	74.2	12.4	3.1	1.5	13.9
September 06, 00:48	25	78.1	13.0	1.5	1.1	14.8
September 03, 00:54	50	45.9	7.7	4.0	1.2	8.8
August 16, 04:24	55	58.7	9.8	<b>21.3</b>	4.7	10.7
August 18, 00:44	55	na	na	na	na	na
September 01, 03:58	55	37.8	6.3	5.0	1.2	10.3
August 26, 00:54	60	46.0	7.7	1.9	0.6	4.6
August 28, 01:33	60	63.9	10.7	2.4	1.1	5.8
August 29, 01:07	60	71.2	11.9	1.2	1.0	6.4
September 06, 00:24	60	44.4	7.4	2.2	0.8	10.9
August 24, 01:12	63	48.3	8.1	5.2	1.4	8.9
August 21, 00:48	65	48.0	8.0	0.4	0.5	7.9
August 16, 03:56	95	35.0	5.8	<b>35.1</b>	7.5	4.2

August 18, 00:17	95	na	na	na	na	na
August 21, 00:22	95	12.9	2.2	0.9	0.2	4.1
August 24, 00:45	95	23.5	3.9	3.8	0.9	3.8
August 26, 00:32	95	18.6	3.1	2.5	0.7	0.2
August 29, 00:44	95	19.5	3.3	2.4	0.5	1.7
September 01, 06:10	95	18.7	3.1	1.3	0.4	5.2
September 03, 00:30	95	14.6	2.4	2.3	0.6	4.3
September 05, 23:59	95	20.7	3.5	1.1	0.4	6.6
August 20, 23:43	195	<b>43.9</b>	7.3	2.0	0.5	<b>5.4</b>
August 16, 03:03	195	<b>32.2</b>	5.4	na	na	3.8
August 17, 23:42	195	na	na	na	na	na
August 29, 00:11	300	9.6	1.6	2.2	0.6	0.0
August 24, 00:08	350	13.1	2.2	2.0	0.4	0.8
August 25, 23:54	350	4.3	0.7	1.7	0.3	0.0
September 01, 06:41	350	<b>32.4</b>	5.4	<b>5.5</b>	0.9	<b>8.5</b>
September 02, 23:58	350	5.6	0.9	1.2	0.2	0.7
August 28, 01:53	500	6.0	1.0	2.0	0.3	0.0
September 05, 00:14	500	5.6	0.9	3.4	0.6	0.9

**Table S6. Concentrations of biogeochemical components of sinking particles after 1, 2 and 4 hours of settling.**

Table illustrates the results of the settling time test. POC, PON, bSi and TEP concentrations (average of replicate filters) and associated uncertainties (standard deviations) measured in sinking particles after 1, 2 and 4 hours of settling. The three marine snow catchers were deployed at two stations at 80 and 60 m, respectively.

Date in 2018 (UTC)	Depth (m)	Settling time (hours)	Sinking POC ( $\mu\text{g L}^{-1}$ )	Sinking PON ( $\mu\text{g L}^{-1}$ )	Sinking bSi ( $\text{nmol L}^{-1}$ )	Sinking TEP ( $\mu\text{g GXeq L}^{-1}$ )
August 20	80	1	$5.4 \pm 1.1$	$0.4 \pm 0.1$	$8 \pm 1$	$0.4 \pm 0.1$
August 20	80	2	$6.1 \pm 0.5$	$0.5 \pm 0.2$	$8 \pm 0$	$0.2 \pm 0$
August 20	80	4	$5.6 \pm 0.7$	$0.7 \pm 0.0$	$8 \pm 0$	$0.3 \pm 0.1$
September 08	60	1	$3.9 \pm 0.2$	$0.5 \pm 0.1$	$12 \pm 3$	$0.4 \pm 0.2$
September 08	60	2	$3.4 \pm 0.1$	$0.4 \pm 0.1$	$10 \pm 2$	$0.1 \pm 0.1$
September 08	60	4	$3.6 \pm 0.2$	$0.6 \pm 0.1$	$15 \pm 1$	$0.2 \pm 0.1$